

# 2D Kinematics and physical properties of $1.0 \lesssim z \lesssim 1.5$ star-forming galaxies\*

M. Lemoine-Busserolle<sup>1</sup>† and F. Lamareille<sup>2</sup>

<sup>1</sup> *Oxford Physics, University of Oxford, Keble Road, Oxford, OX1 3RH, UK*

<sup>2</sup> *Laboratoire d'Astrophysique de Toulouse-Tarbes, Université de Toulouse, CNRS, 14 Avenue E. Belin, F-31400 Toulouse, France*

Accepted 2009 November 20. Received 2009 November 12; in original form 2009 March 6

## ABSTRACT

We combined two-dimensional kinematic and morphology information on the H $\alpha$  emission, obtained using near-infrared integral field spectroscopy, with broad-band photometry to investigate the dynamical structure and the physical properties of a sample of ten late-type galaxies at  $1.0 \lesssim z \lesssim 1.5$ . Their star formation rate ranges from  $\sim 4$  to  $\sim 400 M_{\odot} \text{ yr}^{-1}$  with a mean value of  $\sim 80 M_{\odot} \text{ yr}^{-1}$ . We found that three of these objects are undergoing a strong burst of star formation. The sample displays a range of kinematical types which include one merger, one face-on galaxy, and eight objects showing evidence of rotation. Among these eight objects, half are rotation-dominated galaxies, while the rest are dispersion-dominated. We found also that two galaxies out of the rotation-dominated galaxies are pure rotationally supported disks. They achieve a maximum velocity of  $\sim 180\text{--}290 \text{ km s}^{-1}$  within  $\sim 0.5\text{--}1 \text{ kpc}$ , similar to local spirals with thin disks. Regarding the perturbed rotation and the dispersion-dominated galaxies, they display a plateau velocity range of  $105\text{--}257 \text{ km s}^{-1}$ , which is certainly underestimated due to beam smearing. However, their plateau radii ( $4.5\text{--}10.8 \text{ kpc}$ ) derived from our rotating disk model are significantly higher than those derived for pure rotating disks and local spiral galaxies. The galaxies of our sample have relatively young stellar populations ( $\lesssim 1.5 \text{ Gyr}$ ) and possess a range of stellar mass of  $0.6\text{--}5 \times 10^{10} M_{\odot}$ . In addition, most of them have not yet converted the majority of their gas into stars (six galaxies have their gas fraction  $> 50$  per cent). Therefore, those of them which already have a stable disk will probably have their final stellar mass similar to the present-day spirals, to which these rotating systems can be seen as precursors. We conclude our study by investigating the stellar mass Tully-Fisher relation at  $1.2 \lesssim z \lesssim 1.5$ .

**Key words:** galaxies: evolution – galaxies: formation – galaxies: kinematics and dynamics – galaxies: spiral – galaxies: stellar content – galaxies: starburst

## 1 INTRODUCTION

In the last four years, observations by using integral field spectroscopy (IFS) of individual star-forming galaxies have revealed that galaxies at  $z \gtrsim 1.5$  show a large variety of kinematic and dynamical properties. Recent studies at  $z \sim 1.5 - 1.6$  (Wright et al. 2007, 2009; Bournaud et al. 2008) have confirmed that in addition of the evidence of organized rotation non-negligible random motions are also detected at this redshift. In addition, it appears that large and massive disks with strong star formation already exist at  $z \gtrsim 1.5$

(Förster Schreiber et al. 2006; Genzel et al. 2006, 2008). However more numerous studies at  $z \sim 2 - 3$  (Genzel et al. 2006; Förster Schreiber et al. 2006; Law et al. 2007; Bouché et al. 2007; Genzel et al. 2008; Nesvadba et al. 2008; van Starckenburg et al. 2008; Law et al. 2009) have found an increase in non-circular motions relatives to lower redshift samples. Indeed most of these high-redshift galaxies have high velocity dispersions. Even when a large-scale velocity gradient throughout the galaxy is detected, the value of the ratio of  $V/\sigma$  is relatively low ( $< 10$ ) suggesting that it is unlikely for these galaxies to have a dynamically cold rotating disk of ionised gas similar to the local spiral galaxies ( $V/\sigma \sim 15 - 20$  (Dib et al. 2006)). Most of these ‘heated disks’ appear also to be extremely rich in gas with evidence of high turbulent star formation (Lemoine-Busserolle et al. 2009). Another significant difference in the proper-

\* Based on data obtained with the European Southern Observatory Very Large Telescope, Paranal, Chile, programs 075.A-0318 and 078.A-0177.

† mrlb@astro.ox.ac.uk

**Table 1.** Table of observations

Galaxy	VVDS-ID	RA (J2000)	DEC (J2000)	$z$ (1)	Field (2)	Grating	Exp. Time	Seeing (3)	Run ID
VVDS-1235	020461235	02:26:47.110	-04:23:55.71	1.0351	VVDS-02h	J	1.11h	0''.80	078.A-0177(A)
VVDS-2331	020182331	02:26:44.260	-04:35:51.89	1.2286	VVDS-02h	H	3h	0''.93	078.A-0177(A)
VVDS-6913	220596913	22:14:29.184	+00:22:18.89	1.2667	VVDS-22h	H	1.75h	0''.47	075.A-0318(A)
VVDS-5726	220015726	22:15:42.455	+00:29:03.59	1.3091	VVDS-22h	H	2h	0''.55	075.A-0318(A)
VVDS-4252	220014252	22:17:45.690	+00:28:39.47	1.3097	VVDS-22h	H	2h	0''.61	075.A-0318(A)
VVDS-4103	220544103	22:15:25.708	+00:06:39.53	1.3970	VVDS-22h	J & H	1h (J); 1h (H)	0''.69	075.A-0318(A)
VVDS-4167	220584167	22:15:23.038	+00:18:47.01	1.4637	VVDS-22h	J & H	1h (J); 1.75h (H)	0''.77	075.A-0318(A)
VVDS-7106	020147106	02:26:45.386	-04:40:47.39	1.5174	VVDS-02h	H	2h	0''.89	075.A-0318(A)
VVDS-6027	020116027	02:25:51.133	-04:45:04.48	1.5259	VVDS-02h	H	1.67h	0''.65	075.A-0318(A)
VVDS-1328	020261328	02:27:11.049	-04:25:31.60	1.5291	VVDS-02h	H	1h	0''.61	075.A-0318(A)

The columns are as follows: (1) redshift estimated from optical spectrum obtained with VIMOS, (2) VVDS-22h wide field ( $17.5 \leq I_{AB} \leq 22.5$ ) and VVDS-02h deep field ( $17.5 \leq I_{AB} \leq 24.0$ ), (3) median seeing estimated from the PSF stars (one taken per hour of observation).

ties of some of these high-redshift objects in comparison to the local Universe is the increase in the irregular and asymmetric shape of these galaxies. Although some of these irregular objects may be associated with mergers, the morphology and kinematics of the majority of them are incompatible with being ongoing mergers (Shapiro et al. 2008) and suggest that they are rotationally supported (Genzel et al. 2006; Förster Schreiber et al. 2006; Elmegreen et al. 2007; Genzel et al. 2008). These so-called ‘chain-galaxies’ have the appearance of giant highly clumpy disks. The objects can be kpc wide and as massive as  $10^9 M_{\odot}$  (Elmegreen & Elmegreen 2005; Elmegreen et al. 2009). Elmegreen et al. (2005) was the first to suggest that they could be the progenitor of  $z \sim 1$  spirals. Although the origin of the ‘heated disks’ remains uncertain and highly debated, recent theoretical studies (Dekel et al. 2009a,b) propose a bimodality in galaxy type by  $z \sim 3$  with clumpy star-forming disks and spheroid-dominated galaxies with low star formation rates (SFRs). At  $z \lesssim 1$ , the disks should be stabilized by the dominant stellar disks and bulges, suggested that the redshift region of  $1 < z < 2$  is a crucial step in the formation of massive disk galaxies. Nowadays theoretical studies try to understand the formation and evolution of extended turbulent rotating disks, and observational studies, as the ones presented in this paper, probing the kinematics properties (like observed morphology, dynamical mass, etc), the stellar population properties (age of the population, stellar masses, etc), star forming rates, and the properties of the ionized gas (mass de gas and gas fraction) of the  $1 < z < 2$  disks are mandatory for setting constrains on galaxy formation and evolution.

At lower redshifts, the velocity fields of spiral/rotating disk galaxies have been used to place important constraints on total masses and hence on dark matter halo masses (Conselice et al. 2005). These rotating disks produce a Tully-Fisher relationship (the scaling law between total dynamical mass and the luminous stellar mass) which has apparently not evolved in slope and scatter since  $z \approx 0.6$  (Puech et al. 2006, 2008). Therefore the large scatter found in previously reported Tully-Fisher relationships at moderate redshifts is produced by galaxies with perturbed rotation or complex kinematics. The importance of the role of the non-ordered motion through the gas velocity dispersion for galaxies showing a perturbed rotation was investigated by Weiner et al. (2006) and Kassin et al. (2007). They defined a new tracer of

galaxy-dark halo potential, which combines dynamical support from the rotation with that of the non-ordered motion. The new stellar mass Tully-Fisher relation shows no detectable evolution neither in slope or of its intercept up to  $z \sim 1.2$  (Kassin et al. 2007). Two-dimensional velocity fields allow rotation curves to be deduced in a more robust manner than slit spectra (Weiner et al. 2006). IFS allows pure rotationally-supported disks to be distinguished from other dynamically-disturbed galaxies, which include minor or major mergers, merger remnants and/or inflow/outflows.

In this paper, we explore the kinematic properties of the ionized gas and star formation rates of a sample of ten galaxies at  $1 < z < 1.5$  selected in the VIMOS VLT Deep Survey (VVDS), using integral field unit (IFU)  $H$ -band and  $J$ -band spectroscopy with VLT/SINFONI. The results presented here are part of a study to investigate kinematics and physical properties of unbiased samples representative of the global intermediate and high- $z$  population. This is the second paper of three articles based on data obtained during two observing runs with SINFONI. From the two other companion papers, one (Queyrel et al. 2009) discusses the chemical properties of the intermediate redshift sample presented here and the other presents the results found on the  $z \sim 3$  galaxy sample (Lemoine-Busserolle et al. 2009).

In Section 2 we describe our sample, observational strategy and the data reduction techniques. In Section 3 we address the properties of the nebular emission and also the nature of the stellar population of the galaxies, using broadband photometry to constrain properties such as stellar mass, age and SFRs. In Section 4 we investigate the kinematic structure and dynamical properties inferred from IFS. In Section 5 we explore the nature of these star-forming galaxies and in Section 6 we discuss various relations between the properties of the gas and those of the stellar population and compare our findings with previous studies of the kinematics of intermediate and high-redshift galaxies. Finally in Section 7 we summarize our results and discuss their implications.

We assume a cosmology with  $\Omega_0 = 0.3$ ,  $\Lambda = 0.7$  and  $H_0 = 70 \text{ km s}^{-1} \text{ Mpc}^{-1}$  throughout, and all magnitudes are on the  $AB$  system (Oke & Gunn 1983).

**Table 2.** Nebular emission properties

Galaxy	$z_{H\alpha}$	F(H $\alpha$ ) (1)	L(H $\alpha$ ) (2)	$SFR_{H\alpha}^0$ (3)	E(B-V) $_{gas}$ (4)	$SFR_{corr}$ (5)	$\sigma_{1D}$ (6)	$M_{gas}$ (7)	$\mu$ (8)
VVDS-1235	1.0352	20.1 $\pm$ 2	11.4 $\pm$ 1	5.3 $\pm$ 0.5	0.17 $\pm$ 0.02	8.8 $\pm$ 1	74 $\pm$ 9	8.4 $\pm$ 0.7	0.58 $\pm$ 0.08
VVDS-2331	1.2286	45 $\pm$ 8	39.1 $\pm$ 7	18 $\pm$ 3	0.28 $\pm$ 0.03	42 $\pm$ 8	94 $\pm$ 21	31 $\pm$ 4	0.74 $\pm$ 0.06
VVDS-6913	1.2660	29.7 $\pm$ 3	27.8 $\pm$ 3	12.8 $\pm$ 1	0.09 $\pm$ 0.02	17 $\pm$ 2	113 $\pm$ 18	22 $\pm$ 2	0.34 $\pm$ 0.09
VVDS-5726	1.2927	23.4 $\pm$ 0.3	23.8 $\pm$ 0.3	10.9 $\pm$ 0.1	0.24 $\pm$ 0.02	23 $\pm$ 2	128 $\pm$ 2	19 $\pm$ 1	0.28 $\pm$ 0.07
VVDS-4252	1.3099	201 $\pm$ 54	205 $\pm$ 55	94 $\pm$ 25	0.36 $\pm$ 0.04	280 $\pm$ 83	129 $\pm$ 40	143 $\pm$ 30	0.87 $\pm$ 0.04
VVDS-4103	1.3966	208 $\pm$ 49	248 $\pm$ 59	114 $\pm$ 27	0.42 $\pm$ 0.04	412 $\pm$ 108	107 $\pm$ 57	208 $\pm$ 39	0.93 $\pm$ 0.02
VVDS-4167	1.4656	33.3 $\pm$ 1	44.6 $\pm$ 1	20.5 $\pm$ 0.6	0.10 $\pm$ 0.01	28 $\pm$ 1	141 $\pm$ 6	34.1 $\pm$ 0.8	0.58 $\pm$ 0.08
VVDS-7106	1.5194	21.2 $\pm$ 2	31.1 $\pm$ 3	14.3 $\pm$ 1	0.05 $\pm$ 0.01	16 $\pm$ 2	82 $\pm$ 7	16 $\pm$ 1	0.67 $\pm$ 0.06
VVDS-6027	1.5301	5.63 $\pm$ 0.6	8.4 $\pm$ 0.9	3.85 $\pm$ 0.4	0.00 $\pm$ 0.02	3.9 $\pm$ 0.4	42 $\pm$ 7	5.5 $\pm$ 0.4	0.33 $\pm$ 0.08
VVDS-1328	1.5289	5.48 $\pm$ 0.6	8.2 $\pm$ 0.9	3.76 $\pm$ 0.4	0.01 $\pm$ 0.02	3.9 $\pm$ 0.5	78 $\pm$ 11	5.7 $\pm$ 0.5	0.34 $\pm$ 0.12

The columns are as follows: (1) Flux ( $\times 10^{-17}$  ergs s $^{-1}$  cm $^{-2}$ ), (2) Luminosity ( $\times 10^{41}$  ergs s $^{-1}$ ), (3) raw SFR derived from H $\alpha$ -line ( $M_{\odot}$  yr $^{-1}$ ), (4) reddening suffered by the ionized gas, (5) dereddened SFR, (6) global velocity dispersion derived from H $\alpha$ -line (km/s), (7) total mass of ionized gas ( $10^9 M_{\odot}$ ), (8) gas mass fraction.

## 2 DATA AND OBSERVATIONS

### 2.1 Sample Selection

The 10 galaxies, presented in this paper, were selected in the VVDS-02h “deep” field ( $17.5 \leq I_{AB} \leq 24.0$ ) of the VVDS (Le Fèvre et al. 2005) and in the VVDS-22h “wide” field ( $17.5 \leq I_{AB} \leq 22.5$ ; Garilli et al. 2008). The objects of this sample have spectroscopic redshifts, derived from VLT/VIMOS spectroscopy, between  $z \sim 1.03$  and  $z \sim 1.53$  (see Table 1). Their redshifts are such that the expected wavelengths of the rest-optical H $\alpha$  and [N II] emission lines would be clear of bright OH sky lines in the near-infrared (NIR). These targets were mainly selected on the basis of their measured intensity of [O II]  $\lambda\lambda 3726, 3728$  emission lines in the VIMOS spectra. We chose objects showing the strongest [O II] 3727 emission lines (rest-frame equivalent width (EW)  $> 50$  Å and flux  $> 5 \times 10^{-17}$  ergs $^{-1}$ cm $^{-2}$ ) and having a photometric spectral energy distribution (SED) corresponding to late-type star-forming galaxies.

### 2.2 SINFONI observations

The NIR spectroscopic observations were acquired with the 3D spectrograph SINFONI at ESO-VLT during two 4-nights runs, on 2005 September 5-8 (ESO run 75.A-0318) and 2006 November 12-15 (ESO run 78.A-0177). SINFONI was used in its seeing-limited mode, with the 0.25” pixel scale leading to a field-of-view of  $8 \times 8$  arcsec $^2$ , and the  $H$  grism (1.447 - 1.847  $\mu$ m) providing a spectral resolution  $R \sim 4000$ . One galaxy, VVDS-1235, has been observed with the  $J$  grism (1.098 - 1.399  $\mu$ m), where the detection of the H $\alpha$  emission line is expected. Three galaxies (VVDS-1235, VVDS-4103 and VVDS-4167) have also been observed with the  $J$  grism (1.098 - 1.399  $\mu$ m). Conditions were photometric and the median seeing for each objects, estimated on 2D imaging of point spread function (PSF) stars taken each hour of object observation, is indicated in Table 1. Observing strategy and data reduction have been described in Lemoine-Busserolle et al. (2009).

## 3 SPECTROPHOTOMETRY PROPERTIES

### 3.1 Nebular integrated emission properties

#### 3.1.1 One-dimensional spectral properties of H $\alpha$ emission

Integrated rest-frame optical one-dimensional spectra were extracted from the SINFONI data cube for each object. From these 1D spectra, we measured line fluxes and linewidths of the integrated H $\alpha$  line emission (see Fig. 1). Using the IRAF task ‘splot’, we derived the systemic redshift  $z_{H\alpha}$ , the total H $\alpha$  flux and the global velocity dispersion  $\sigma_{1D}$  (corrected for the instrumental resolution of  $\sim 6.5$  Å in the  $J$  band and  $\sim 6.8$  Å in the  $H$  band). Table 2 list the properties of the nebular emission of the 10 galaxies of our sample. It is interesting to note that all our targets, except VVDS-6027, have a value of  $\sigma_{1D} > 70$  km s $^{-1}$ .

#### 3.1.2 Star Formation rates from H $\alpha$ emission

The H $\alpha$  nebular recombination line is a direct probe of the young, massive stellar population and therefore provides a nearly instantaneous (i.e. averaged on the last ten million years) measure of the SFR. The H $\alpha$  line is moreover not strongly affected by dust extinction. We have calculated  $SFR_{H\alpha}$  following the Kennicutt (1998) calibration, re-normalized to Chabrier (2003) IMF:

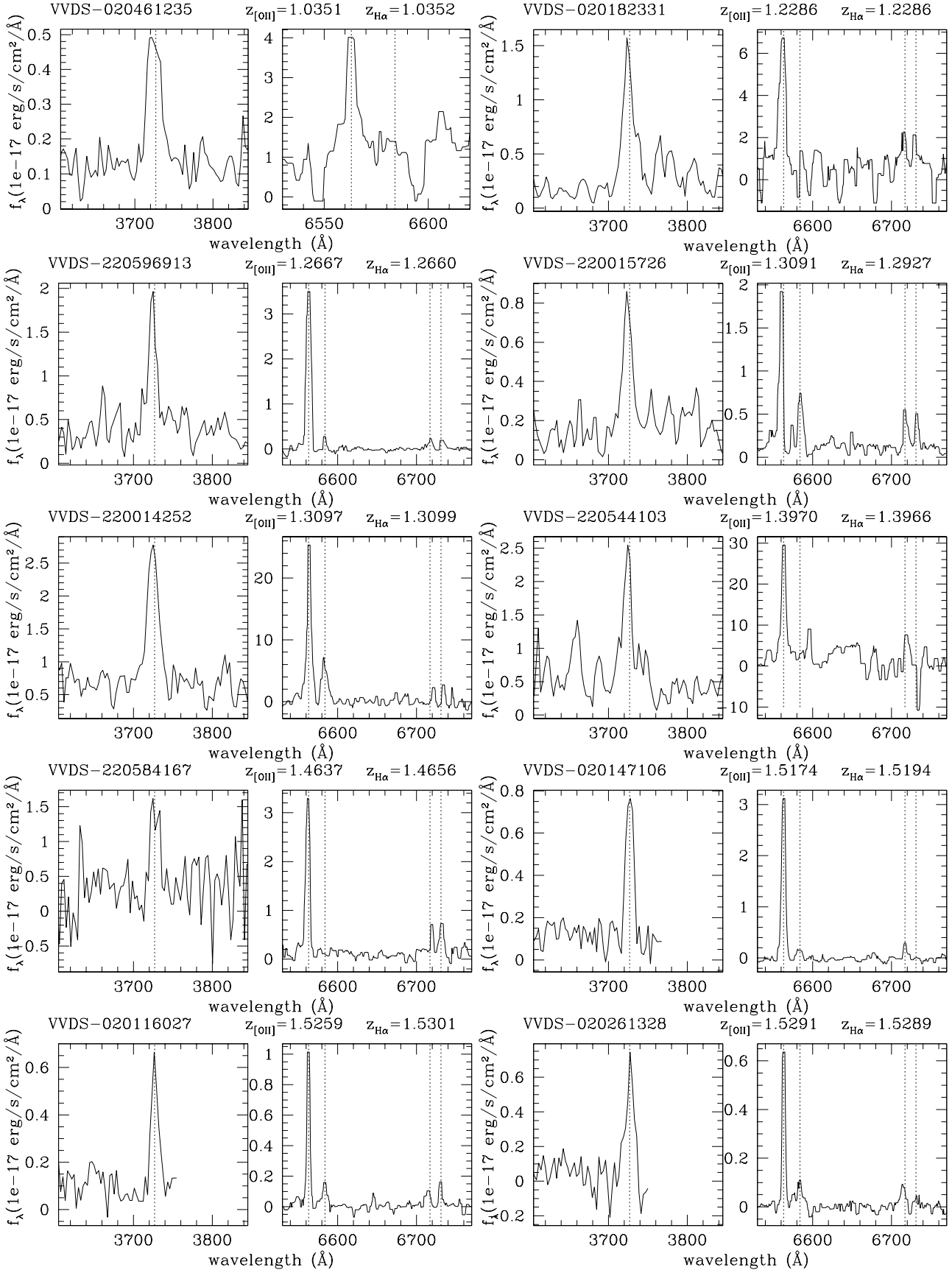
$$SFR_{H\alpha} (M_{\odot} \text{ yr}^{-1}) = 4.6 \times 10^{-42} L(H\alpha) \text{ (erg s}^{-1}\text{)}. \quad (1)$$

Table 2 list the star formation rates deduced from the H $\alpha$  emission for the 10 galaxies of our sample. We found that the non-dust-corrected  $SFR_{H\alpha}$  is between  $\sim 4 - 114 M_{\odot} \text{ yr}^{-1}$ , with seven of our galaxies with a  $SFR_{H\alpha} > 10 M_{\odot} \text{ yr}^{-1}$ . These high SFRs are expected, taking into account our selection criteria for the [O II] flux (see section 2.1).

### 3.2 Stellar population properties

#### 3.2.1 Spectral Energy Distribution and best-fit models

We derived the spectral energy distributions (SED) of our 10 galaxies from broad-band photometry. The magnitudes in  $BVRI$  filters obtained with the CFH12k camera on CFHT (McCracken et al. 2003; Le Fèvre et al. 2004) were extracted from the VVDS catalog <http://cencosw.oamp.fr> (Iovino et al. 2005; Temporin et al. 2008), and magnitudes in  $ugriz$



**Figure 1.** One-dimensional rest-frame spectra for the 10 galaxies of our sample obtained with VIMOS (left) and with SINFONI (right), in optical and in  $H$ -band (or  $J$ -band for VVDS-1235) respectively. The position of the following lines are shown by a vertical line, from left to right: [OII] $\lambda$ 3727, [NII] $\lambda$ 6584, [SII] $\lambda$ 6717, and [SII] $\lambda$ 6731. The redshifts inferred from [OII] $\lambda$ 3727 and from  $H\alpha$  lines are indicated in the title of each plots.

**Table 3.** Photometric data and Spectral energy distributions

Galaxy	$B_{AB}$	$V_{AB}$	$R_{AB}$	$I_{AB}$	$u_{AB}$	$g_{AB}$	$r_{AB}$	$i_{AB}$	$z_{AB}$	$J_{AB}$	$K_{AB}$
VVDS-1235	$24.1 \pm 0.06$	$23.7 \pm 0.05$	$23.4 \pm 0.05$	$22.6 \pm 0.05$	$24.1 \pm 0.03$	$23.8 \pm 0.02$	$23.5 \pm 0.02$	$22.8 \pm 0.01$	$22.7 \pm 0.04$	$22.3 \pm 0.05$	$21.8 \pm 0.06$
VVDS-2331	$24.0 \pm 0.09$	$23.6 \pm 0.07$	$23.4 \pm 0.07$	$22.7 \pm 0.06$	$24.0 \pm 0.03$	$23.6 \pm 0.02$	$23.2 \pm 0.02$	$22.9 \pm 0.01$	$22.3 \pm 0.03$	$22.3 \pm 0.10^*$	$21.6 \pm 0.11$
VVDS-6913	-	-	-	$21.7 \pm 0.14$	$23.1 \pm 0.02$	$22.6 \pm 0.01$	$22.3 \pm 0.01$	$22.1 \pm 0.01$	$21.3 \pm 0.00$	-	-
VVDS-5726	-	-	-	$22.4 \pm 0.17$	$24.3 \pm 0.04$	$23.6 \pm 0.02$	$23.2 \pm 0.01$	$22.7 \pm 0.01$	$22.1 \pm 0.01$	-	-
VVDS-4252	$22.5 \pm 0.03$	$22.4 \pm 0.02$	$22.1 \pm 0.01$	$22.0 \pm 0.17$	$22.9 \pm 0.01$	$22.4 \pm 0.01$	$22.1 \pm 0.01$	$22.0 \pm 0.00$	$21.5 \pm 0.00$	$21.5 \pm 0.08^*$	$21.0 \pm 0.08^*$
VVDS-4103	-	-	-	$22.3 \pm 0.17$	$23.2 \pm 0.02$	$22.7 \pm 0.01$	$22.4 \pm 0.01$	$22.3 \pm 0.01$	$22.1 \pm 0.01$	-	-
VVDS-4167	-	-	-	$21.9 \pm 0.10$	-	-	-	-	-	-	$21.3 \pm 0.20^*$
VVDS-7106	$22.9 \pm 0.04$	$22.8 \pm 0.04$	$22.7 \pm 0.04$	$22.5 \pm 0.04$	$23.0 \pm 0.01$	$22.7 \pm 0.01$	$22.6 \pm 0.01$	$22.5 \pm 0.01$	$22.4 \pm 0.02$	$22.0 \pm 0.15^*$	$22.1 \pm 0.15^*$
VVDS-6027	$23.6 \pm 0.07$	$23.2 \pm 0.05$	$23.1 \pm 0.05$	$22.9 \pm 0.08$	$24.0 \pm 0.04$	$23.4 \pm 0.02$	$23.3 \pm 0.02$	$23.1 \pm 0.02$	$22.8 \pm 0.05$	$22.6 \pm 0.50^*$	$23.2 \pm 0.50^*$
VVDS-1328	$24.3 \pm 0.07$	$24.1 \pm 0.06$	$24.2 \pm 0.08$	$23.9 \pm 0.12$	$24.2 \pm 0.04$	$23.8 \pm 0.03$	$23.6 \pm 0.03$	$23.5 \pm 0.03$	$23.6 \pm 0.10$	$23.1 \pm 0.20$	$22.2 \pm 8.03$

\*: magnitudes from the UKIDSS survey.

**Table 4.** Stellar population properties

Galaxy	$M_\star$ (1)	$L_{1500}$ (2)	$SFR_{UV}^0$ (3)	$SFR_{sed}$ (4)	$E(B-V)_{sed}$ (5)	age (6)
VVDS-1235	$6 \pm 2$	$2.3 \pm 0.2$	$1.8 \pm 0.2$	$11 \pm 5$	$0.28 \pm 0.12$	$0.68 \pm 0.3$
VVDS-2331	$11 \pm 3$	$3.7 \pm 0.1$	$3 \pm 0.1$	$27 \pm 14$	$0.32 \pm 0.11$	$0.54 \pm 0.3$
VVDS-6913	$43 \pm 16$	$8.7 \pm 0.4$	$7.1 \pm 0.4$	$49 \pm 22$	$0.28 \pm 0.10$	$0.96 \pm 0.5$
VVDS-5726	$50 \pm 17$	$3.1 \pm 0.4$	$2.4 \pm 0.4$	$42 \pm 28$	$0.37 \pm 0.13$	$1.26 \pm 0.7$
VVDS-4252	$21 \pm 7$	$11.2 \pm 0.3$	$9.4 \pm 0.2$	$73 \pm 26$	$0.28 \pm 0.08$	$0.40 \pm 0.2$
VVDS-4103	$16 \pm 4$	$9.4 \pm 0.5$	$7.7 \pm 0.4$	$91 \pm 49$	$0.28 \pm 0.03$	$1.75 \pm 1.6$
VVDS-4167	$25 \pm 8$	$12.5 \pm 0.5$	$10.6 \pm 0.4$	$129 \pm 46$	$0.29 \pm 0.07$	$0.29 \pm 0.1$
VVDS-7106	$8 \pm 2$	$12.9 \pm 0.1$	$10.6 \pm 0.1$	$44 \pm 11$	$0.16 \pm 0.04$	$0.27 \pm 0.1$
VVDS-6027	$11 \pm 4$	$5.1 \pm 0.2$	$4.1 \pm 0.2$	$33 \pm 12$	$0.24 \pm 0.08$	$0.46 \pm 0.3$
VVDS-1328	$11 \pm 6$	$4.4 \pm 0.2$	$3.5 \pm 0.2$	$14 \pm 6$	$0.19 \pm 0.11$	$0.88 \pm 0.6$

The columns are as follows: (1) Stellar mass ( $10^9 M_\odot$ ), (2) Luminosity at  $1500\text{\AA}$  ( $\times 10^{+28}$  ergs  $\text{s}^{-1}$   $\text{Hz}^{-1}$ ), (3) raw SFR derived from UV luminosity ( $M_\odot \text{ yr}^{-1}$ ), (4) dereddened SFR derived from the full SED (averaged in the last  $10^8$  years), (5) reddening suffered by the stars, (6) age of the oldest stellar populations (Gyr).

filters from the CFHTLS T003 release (Ilbert et al. 2006). Finally, we have also used magnitudes in  $J$  and  $K$  bands from the UKIDSS survey (Lawrence et al. 2007). All the photometric data are presented in Table 3.

Table 4 list the properties of the stellar population for the sample of the 10 galaxies derived from the SEDs. The stellar masses, the reddening suffered by stars, and the ages of the oldest stellar populations are estimated thanks to the full optical and near-infrared photometry available for our targets. The photometric points are compared to those of a library of synthetic stellar population spectra based on the latest 2007 models of Charlot & Bruzual (Bruzual 2007, latest models in preparation) models, using the Chabrier (2003) IMF. The synthetic stellar populations are based on exponential declining star formation histories with the addition of random secondary bursts. We calculated the probability distribution function as  $e^{-\chi^2}$  for each observed galaxy compared to all models in the library. We take as an estimate of the stellar mass the median of this distribution. The results are self-consistently corrected for the effects of age, metallicity and dust. Degeneracies between these parameters are reflected in the error bars of the derived quantities. Fig. 2 shows the comparison between the observed SEDs and our best-fitting stellar population models.

### 3.2.2 Star formation rates from photometry

Ultraviolet-derived star formation rates were calculated from the  $u$ -band photometry (see Table 3). Given the redshift of our targets, the  $u$ -band is sensitive to the rest-frame UV continuum flux around  $1500 \text{\AA}$ ; in the absence of dust,

the UV continuum from a young stellar population is approximately flat if the flux is expressed in frequency units ( $f_\nu$ ). The mean luminosity in frequency units (ergs  $\text{s}^{-1}$   $\text{Hz}^{-1}$ ) is calculated using the following equation:

$$L_{1500} = 10^{(-0.4 \cdot m(AB))} \times 3631 \cdot 10^{-23} \times 4\pi \frac{D_{L(cm)}^2}{1+z}. \quad (2)$$

We can then deduce  $SFR_{UV}$  using the following :

$$SFR_{UV}(M_\odot \text{ yr}^{-1}) = 0.83 \times 10^{-28} L_{1500} (\text{ergs s}^{-1} \text{ Hz}^{-1}). \quad (3)$$

This equation is the Kennicutt (1998) calibration renormalized from Salpeter (1955) to Chabrier (2003) IMF. Table 4 list the value of the star formation rate computed from the UV rest-frame continuum emission.

Additionally the star formation rates, averaged on the last hundred million years,  $SFR_{SED}$ , can be also derived from the full SEDs using the same approach as for the stellar masses, reddening, and ages. They are also indicated in Table 4 for the 10 galaxies of our sample.

### 3.3 Reddening and dust corrected star formation rate

The UV star formation rates may be strongly affected by extinction, its comparison with the  $H\alpha$  star formation rate may thus provide an estimate of the amount of dust. Assuming that all of the ionizing photons are reprocessed into nebular lines, therefore  $SFR_{H\alpha}^{corr} = SFR_{UV}^{corr}$  after correction for dust extinction, we thus computed the  $E(B-V)$  by solving the following system of two equations:

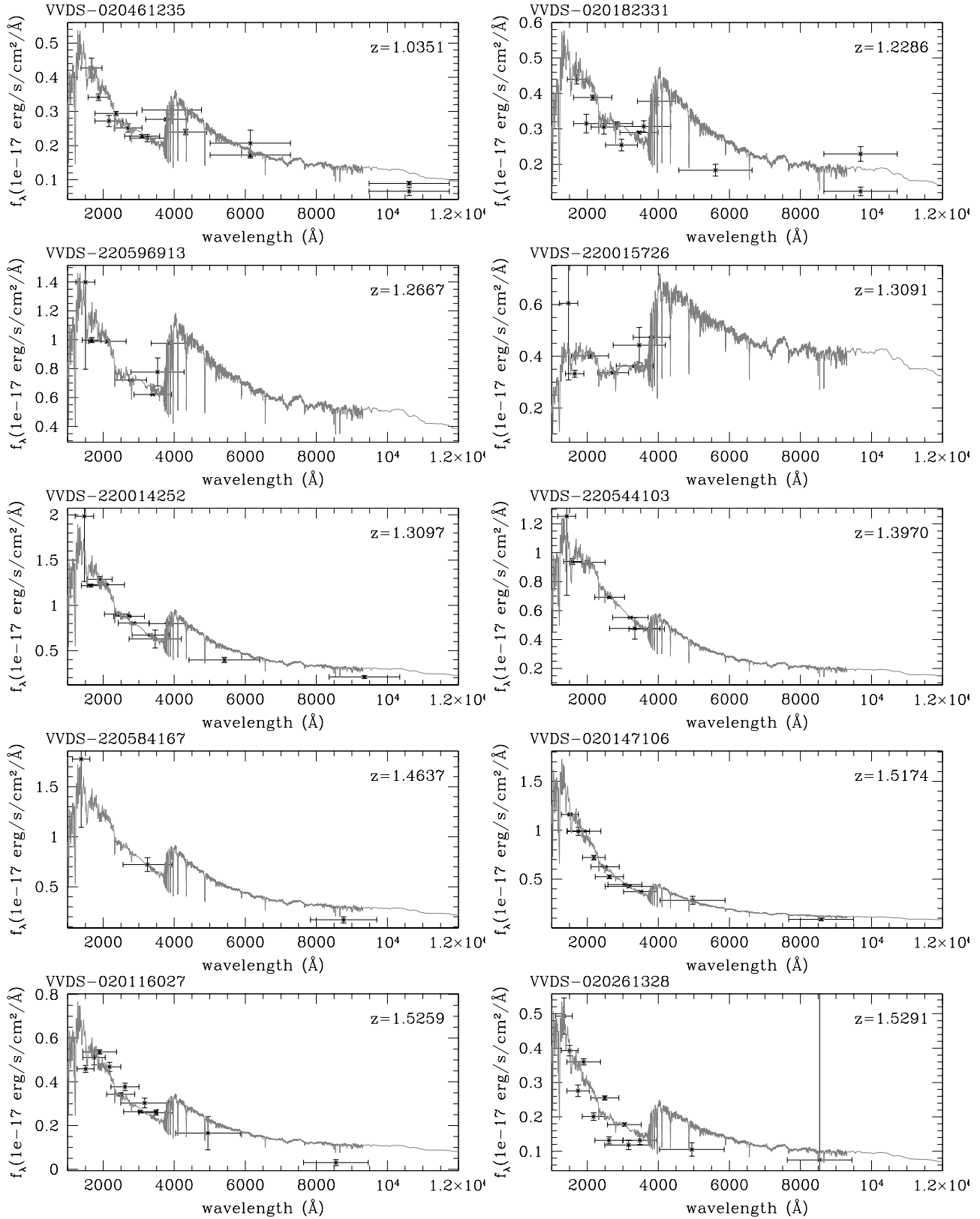


**Figure 2.** Rest-frame SEDs from the broad-band CFHT optical and near-infrared NTT/SOFI (or UKIDSS) photometry for our sample of 10 galaxies (see also Table 3). The best-fitting stellar population model is overlaid.

$$\begin{aligned} SFR_{corr} &= SFR_{H\alpha} \cdot 10^{0.4E(B-V)_{gas}} k^e(0.6563) \\ SFR_{corr} &= SFR_{UV} \cdot 10^{0.4E(B-V)_{gas}} k^e(0.1500), \end{aligned} \quad (4)$$

where the obscuration curve for the ionized gas,  $k^e(\lambda)$ , is given by Calzetti (2001):

$$\begin{aligned} k^e(\lambda) &= 2.659(-2.156 + 1.509/\lambda - 0.198/\lambda^2 \\ &\quad + 0.011/\lambda^3) + 4.05 \\ &\quad 0.12 \mu m \leq \lambda < 0.63 \mu m, \\ k^e(\lambda) &= 2.659(-1.857 + 1.040/\lambda) + 4.05 \\ &\quad 0.63 \mu m \leq \lambda \leq 2.20 \mu m. \end{aligned} \quad (5)$$

We, then, derived the dereddened star formation rate,  $SFR_{corr}$ , listed in Table 2.

### 3.4 Gas mass and gas mass fraction

The relation between the star formation surface density  $\Sigma_{SFR}$  (in  $M_\odot \text{ yr}^{-1} \text{ kpc}^{-2}$ ) and the gas surface density  $\Sigma_{gas}$  (in  $M_\odot \text{ pc}^{-2}$ ) is given by the Schmidt law (Kennicutt 1998):

$$\Sigma_{SFR} = 1.48 \cdot 10^{-4} \times (\Sigma_{gas})^{1.4}, \quad (6)$$

which has been renormalized to the Chabrier (2003) IMF. We thus calculate the star formation surface density by dividing the dereddened star formation rate ( $SFR_{corr}$ ) by the projected area of the galaxy (see Table 5). We used the two-dimensional  $H\alpha$  emission distribution, deconvolved with the point spread function (PSF), to directly estimate the spatial extend of the ionized gas,  $A_{gas}$ , so that  $M_{gas} = A_{gas} \times \Sigma_{gas}$ .

We then calculate the gas surface density by inverting the above equation, and finally calculate the gas mass by multiplying the gas surface density with the projected area. We also derived the gas mass fraction, which is  $\mu = M_{gas}/(M_{gas} + M_*)$ , where  $M_*$  is the stellar masses deduced from the SED modelling. The gas mass and the gas mass fraction are given in Table 2. We found that six of our galaxies have high values of the gas fraction ( $\mu > 0.5$ ).

### 3.5 Virial mass

While the global velocity dispersion  $\sigma_{1D}$  alone does not allow us to distinguish between any systematic velocity shift across the galaxy and any random motions, it can provide a reasonable estimate of the mass of the object. Assuming a virialized motion around the morphological galaxy centre, we can use this  $\sigma_{1D}$  as a crude estimate of the mass within the largest radius  $r_{gas}$  (estimated from the  $2\sigma$  width of the  $H\alpha$  flux profile along the major axis and deconvolved with the seeing, see Table 5) for which a velocity is measured using the formula:

$$M_{vir}(\sigma_{1D}) = \frac{C\sigma_{1D}^2 r_{gas}}{G} \quad (7)$$

(where  $C = 3.4$  for of a gas-rich disk with an average inclination angle; see Erb et al. (2006b)). In Table 7 we indicate dynamical masses inferred from the  $\sigma_{1D}$ . The values span a range from  $\sim 1\text{-}26 \times 10^{10} M_\odot$ , with four galaxies having a virial mass  $> 1 \times 10^{11} M_\odot$

## 4 PROPERTIES FROM SPATIALLY RESOLVED KINEMATICS

### 4.1 $H\alpha$ kinematics

We produced two-dimensional maps of the dynamics for the galaxies in our sample by using E3D, the Euro3D visualization tool (Sánchez et al. 2004), and a code for the fitting and analysis of kinematics (e.g. Sánchez et al. 2004, 2005). Our main goal was to determine the kinematics of the ionised gas using the strongest emission line,  $H\alpha$ . For each spatial pixel (spaxel) we fit the  $H\alpha$  emission line profile with a single Gaussian function, in order to characterize the emission line, and a pedestal to characterise any spectral continuum. We first smoothed the reduced cubes spatially with a Gaussian of  $\text{FWHM} = 3$  pixels ( $0''.37$ ). The line flux, FWHM, central wavelength and the continuum (pedestal) were then fitted. From the results of this fitting we obtained maps (see Fig. 3 and Fig. 4) of the  $H\alpha$  emission line intensity, the relative radial velocity map ( $V_r$ ) and the velocity dispersion ( $\sigma$ ). The dispersion map was corrected for the contribution of the instrumental dispersion, as determined from the FWHM of unblended and unresolved sky lines. Error maps for the velocity and dispersion measurements were also computed. The errors are dominated by the effect of random noise in fitting the line profile which produces large errors at low S/N. Errors ranged from 4 to 25  $\text{km s}^{-1}$  for both the radial velocity and velocity dispersion maps.

### 4.2 Gas morphology

Fig. 3 and Fig. 4 contain images of the  $H\alpha$  emission line intensity for each of the galaxies. We also plot the morphology of the stellar component mapping by the CFTHLS  $I$ -band continuum. Nine of the objects have a distinct single peak in the  $H\alpha$  distribution. This peak emission of the star formation from  $H\alpha$  is coincident (or near-coincident) with the peak stellar continuum emission in the  $I$  band. Only one of the targets, VVDS-1235, has distinct resolved knot-like structures in the  $H\alpha$  distribution which are not seen in the stellar emission.

Given the similarity between the distribution of the  $H\alpha$  flux in our IFU observations and the continuum in the optical images, we decided to use our line flux maps, which have the better resolution, to infer the morphological parameters: the centre (as defined by the position where the flux is maximum); the position angle (PA), and the inclination. The inclination is calculated as  $\cos^{-1}(b/a)$ , where  $a$  and  $b$  are the radius of major and minor axis, respectively, which are measured as the  $1\sigma$  profile of the flux map. The distance between the kinematical and the morphological centres is given in Table 5. We also measure a kinematical PA in case it is slightly offset from the morphological PA. The kinematical PA can be measured in two consistent ways: or we look for the major axis as the direction where the velocity gradient is maximum, or we look for the minor axis as the direction where the velocity gradient is minimum. The difference between the kinematical and morphological PAs is given in Table 5.

**Table 5.** Morphological parameters and initial guesses for the rotation modelling.

Galaxy	$\Delta c$ (a)	PA (b)	$\Delta PA_{gas}$ (c)	$i$ (d)	$r_{gas}$ (e)	$A_{gas}$ (f)
VVDS-1235	-	42°*	-	70°	$9.8 \pm 1.4$	63
VVDS-2331	2.4	-69°	-41°	52°	$9.2 \pm 1.6^\ddagger$	120
VVDS-6913	8.5	-99°	-4°	63°	$20.2 \pm 0.8$	348
VVDS-5726	1.7	-18°	-10°	24°	$6.7 \pm 1.0$	112
VVDS-4252	1.8	45°	-3°	50°	$10.6 \pm 1.1$	225
VVDS-4103	2.6	-167°	-18°	53°	$13.4 \pm 1.2$	315
VVDS-4167	2.8	162°	-10°	62°	$16.6 \pm 1.4$	468
VVDS-7106	0.0	-119°	0°	37°	$7.7 \pm 1.6$	142
VVDS-6027	-	175°*	-	41°	$6.9 \pm 1.1$	108
VVDS-1328	1.2	-27°	30°	20°	$7.1 \pm 1.1$	127

The columns are as follows: (a) distance between the maximum of H $\alpha$  distribution and the kinematic centre (kpc); (b) initial guess kinematic position angle; (c) difference between the morphological (inferred from the H $\alpha$  distribution) and kinematic position angles; (d) inclination inferred from the H $\alpha$  distribution (0° for face-on); (e) *2sigma* profile of H $\alpha$  distribution map along the major axis (kpc). Uncertainty represents half of the PSF correction; (f) projected area of the nebular emission (kpc<sup>2</sup>).

\*: for objects which do not show a rotation, we give the morphological PA.

‡: for VVDS-2331, we give the radius calculated with respect to the morphological major axis, not the kinematical major axis.

**Table 6.** Best-fit parameters from the rotation modelling.

Galaxy	$PA_{mod}$ (a)	$i_{mod}$ (b)	$\sigma_0$ (c)	$V_s$ (d)	$V_{rot}$ (e)	$r_c$ (f)	res(v) (g)	res(d) (h)
VVDS-2331	$-64^\circ \pm 21$	$51^\circ \pm 33$	$38 \pm 41$	$-8 \pm 21$	$193 \pm 72$	$4.8 \pm 8$	$-1 \pm 43$	$11 \pm 34$
VVDS-6913	$-113^\circ \pm 28$	$62^\circ \pm 19$	$44 \pm 22$	$-6 \pm 19$	$139 \pm 30$	$10.7 \pm 3$	$-2 \pm 30$	$20 \pm 23$
VVDS-5726	$-6^\circ \pm 22$	$24^\circ \pm 7$	$60 \pm 35$	$-17 \pm 15$	$292 \pm 71$	$1.5 \pm 2$	$-2 \pm 25$	$5 \pm 19$
VVDS-4252	$32^\circ \pm 11$	$48^\circ \pm 15$	$100 \pm 12$	$-2 \pm 7$	$130 \pm 23$	$4.5 \pm 2$	$4 \pm 10$	$0 \pm 11$
VVDS-4103	$167^\circ \pm 23$	$79^\circ \pm 5$	$58 \pm 37$	$-10 \pm 12$	$118 \pm 27$	$8.5 \pm 3$	$-2 \pm 20$	$1 \pm 28$
VVDS-4167	$-176^\circ \pm 16$	$72^\circ \pm 23$	$54 \pm 25$	$-11 \pm 12$	$257 \pm 34$	$10.8 \pm 2$	$2 \pm 14$	$5 \pm 18$
VVDS-7106	$-134^\circ \pm 35$	$37^\circ \pm 26$	$82 \pm 6$	$7 \pm 6$	$105 \pm 71$	$9.4 \pm 4$	$2 \pm 7$	$-2 \pm 10$
VVDS-1328	$-10^\circ \pm 25$	$20^\circ \pm 7$	$36 \pm 17$	$17 \pm 10$	$182 \pm 56$	$0.5 \pm 4$	$-1 \pm 11$	$7 \pm 17$

The columns are as follows: (a) position angle (b) inclination (c) local velocity dispersion (km s<sup>-1</sup>) (d) systemic velocity (km s<sup>-1</sup>) (e) maximum velocity (km s<sup>-1</sup>) (f) radius where the maximum velocity is reached (kpc) (g) mean value and rms of the residual velocity map (km s<sup>-1</sup>) (h) mean value and rms of the residual dispersion map (km s<sup>-1</sup>).

### 4.3 Rotation modelling

Each galaxy is modelled by a pure, infinitely thin, rotating disk. The parameters of the model are the kinematic centre  $(x_0, y_0)$ , the position angle (PA), the inclination ( $i$ ), the velocity offset ( $V_s$ ) of the centre relative to the integrated spectrum, and the velocity curve  $V_c(r)$  where  $r$  is the radius from the kinematic centre. We also use the true physical velocity dispersion  $\sigma_0$  as a model parameter, which we assume is constant, and represents the thickness of the rotating disk. Below its maximum, the velocity is assumed to increase linearly with the radius and then remain constant (Wright et al. 2007). The radial velocity  $V$  for any point is then defined with standard projection equations. Note that the PA gives the direction of positive radial velocities. The velocity offset accounts for redshift uncertainties. We define the velocity curve by two parameters, following Wright et al. (2007): the maximum velocity  $V_{max}$  and the radius  $r_c$  where this maximum velocity is achieved. In this model, below  $r_c$  the velocity is defined as:

$$V_c(r) = \frac{r}{r_c} \times V_{max} \quad (8)$$

The model computes  $V_{rot}$ , the asymptotic maximum rotation velocity at the plateau of the rotation curve, corrected for inclination ( $V_{rot} = V_{rot} / \sin i$ ).

In reality, the spatial resolution is limited by the seeing and the spaxel size. The observed radial velocity is thus the weighted convolution of the true radial velocity by the PSF. This PSF is modelled as a 2D Gaussian and takes into account the 3-pixel spatial smoothing. The weights come from the flux map of the line used to compute the velocity map: a spaxel where the observed line flux is negligible will not contribute to the convolution. Additionally, the observed velocity dispersion accounts not only for the true physical dispersion, but also for the variations in the velocity field inside the width of the PSF. We generate a map of the velocity dispersion where the velocity gradient (determined from the modelling) has been subtracted. This yields a better measure of the intrinsic local velocity dispersion, rather than a raw value of  $\sigma$  which may be inflated if the velocity gradient across a spaxel is large. From this map, we compute the flux-weighted mean velocity dispersion,  $\sigma_o$  (Table 6).

The beam smearing introduced by the PSF causes two significant effects. First, the observed velocity map appears smoothed, therefore the velocity gradient and the maximum velocity are underestimated. Secondly, the observed dispersion map shows a peak of dispersion near to the kinematic centre. We can reproduce modelled velocity and dispersion maps by applying mathematically the same weighted convolution to the ideal velocity field. A better modelling of the beam smearing would be to convolve our modelled veloc-

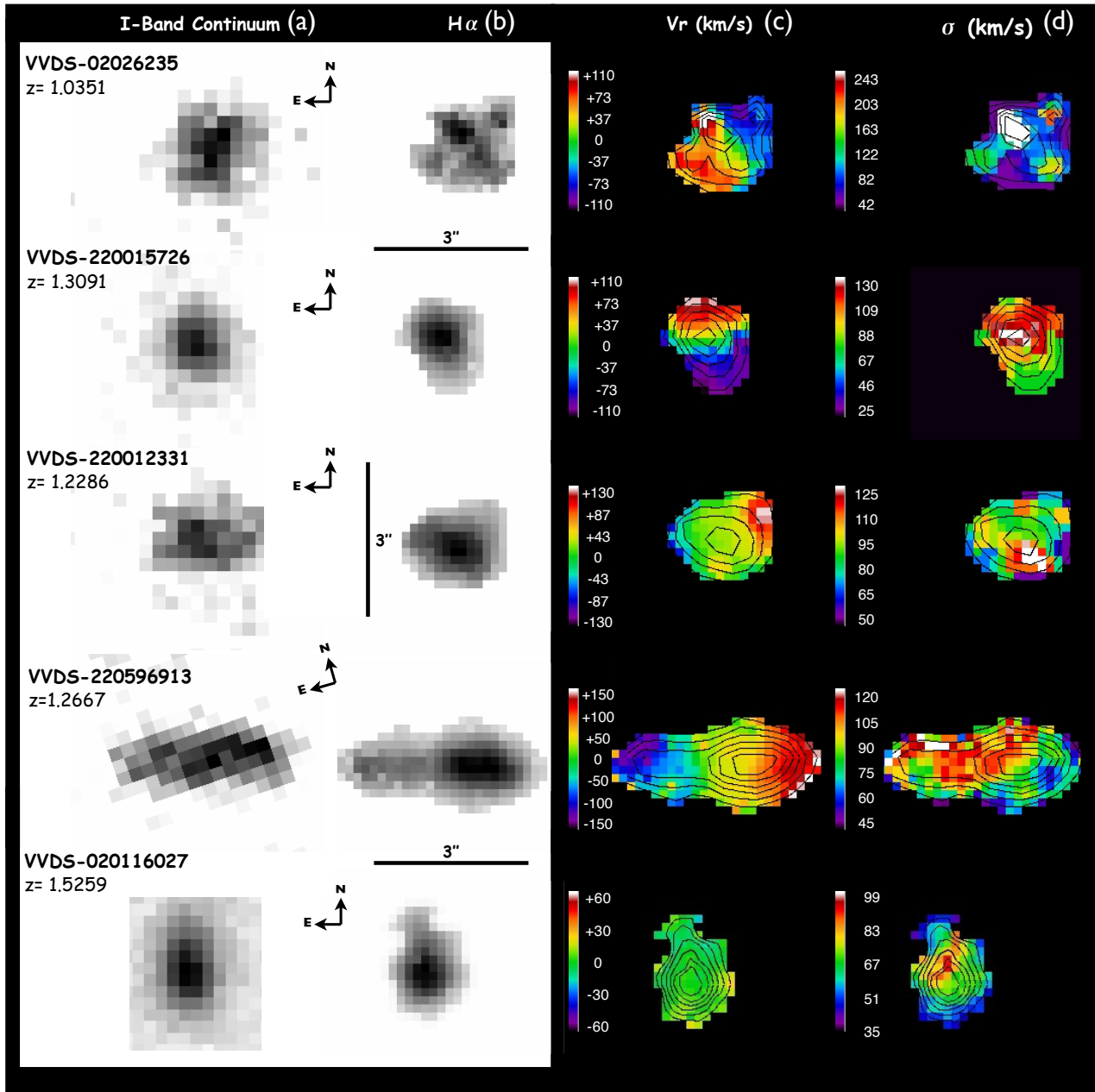


**Figure 3.** From left to right: (a)  $I$ -band CFHT image, (b)  $H\alpha$  flux map, (c)  $H\alpha$  velocity field, and (d)  $H\alpha$  velocity dispersion map obtained from Gaussian fits to the SINFONI data cubes after smoothing spatially with a two-dimensional Gaussian of FWHM = 3 pixels. The  $I$ -band image and  $H\alpha$  maps are color-coded with a linear scaling such that the values increase from light to dark. These data have been acquired with the  $125 \times 250$  mas sampling configuration of SINFONI, in seeing limited mode. An angular size of  $1''$  corresponds to  $\sim 8$  kpc at the redshifts of most of the objects. The direction of North-East, the VVDS number identification and VIMOS-based redshift are indicated for each galaxy.

ity and dispersion maps with the PSF in each wavelength channel, weighted by the intrinsic flux distributions of the systems at this wavelength (Emsellem, Monnet, & Bacon 1994). However, for such high redshift galaxies for which the intrinsic flux distributions is unknown and taking into account the quality of the data, it is not possible to model the velocity and dispersion maps to such a high precision. The modelled maps are compared to the observed maps by a  $\chi^2$ -minimization. The parameters which minimize the  $\chi^2$  are computed in two successive grids with increasing resolu-

tion. First guesses for the kinematic centre, the PA, and the inclination are set from the morphology.

#### 4.4 Dynamical classes, masses and disk stability

In order to characterize the galaxies in our sample, we used a kinematical classification based on the comparison of the morphology of the stars (showing by the CFHT  $i$ -band image) with the morphology of the  $H\alpha$  flux distribution. We classified the galaxies through analysis of the observed ve-

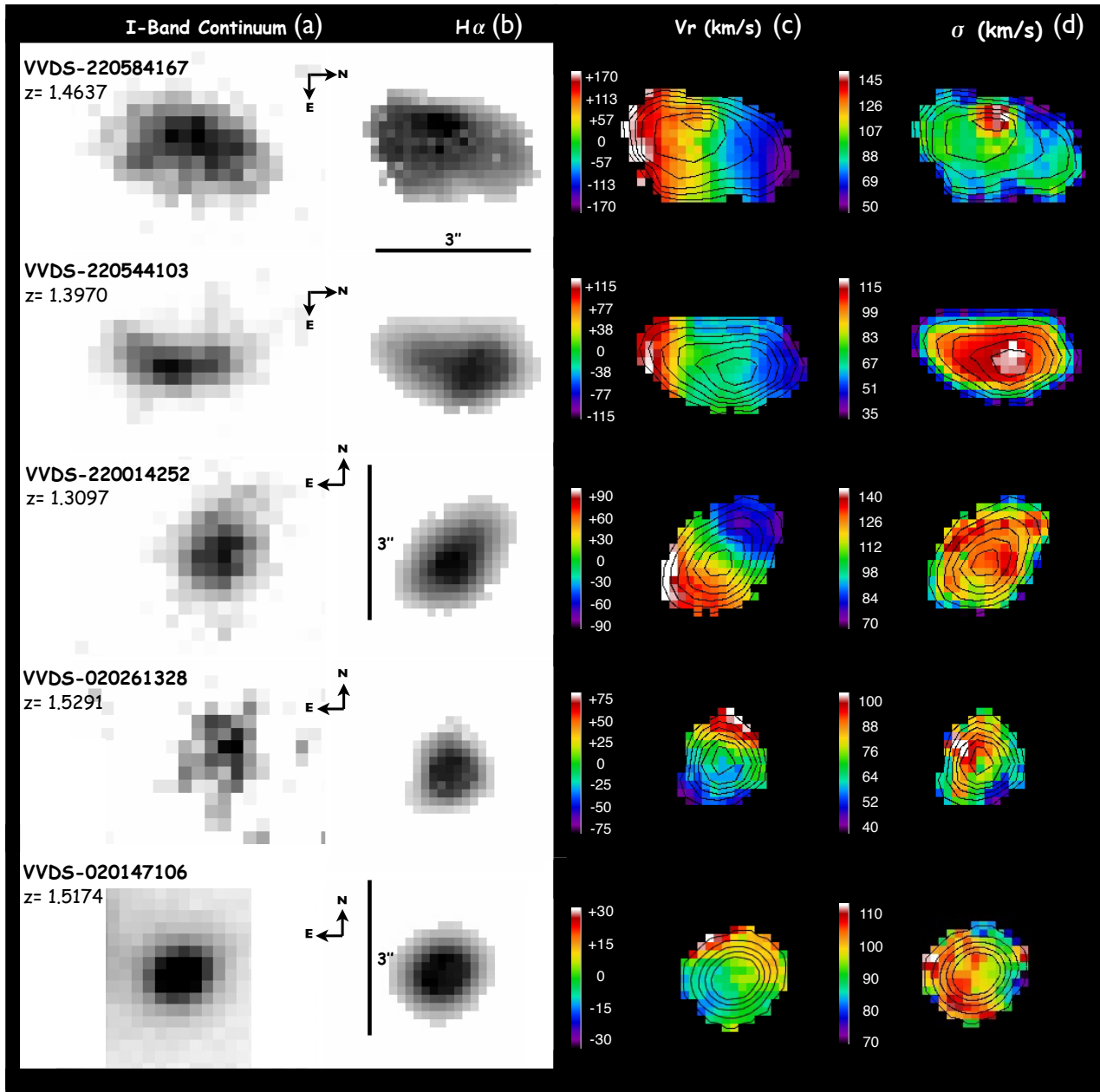


Figure 4. Similar as Fig.3 for five other galaxies.

locity map, the observed velocity dispersion map ( $\sigma$ , corrected from the instrumental effect), and the velocity residuals map.

On the 10 galaxies of our sample, only two objects present a dynamical structure which is not compatible with rotation and which has not been successfully fitted by the simple rotating disk model. One object, VVDS-1235, has a complex kinematics with multiple velocity shear and several peak regions in the  $\sigma$ -map, and we defined as a *merger* and the other, VVDS-6027, shows negligible velocity shear (defined as *featureless*, with the possibility of being a face-on disk). The remaining eight objects appear compatible with rotating disks and we used the correlation between the integrated line width,  $\sigma_{1D}$ , and the maximum velocity dispersion estimated by the best-fitting rotating model to dis-

tinguish rotation-dominated (RD) galaxies from dispersion-dominated (DD) galaxies (Weiner et al. 2006). Fig. 5 shows that four galaxies of our sample (VVDS-2331, VVDS-5726, VVDS-4167, and VVDS-1328) are RD disk (open circle) and four others (VVDS-4252, VVDS-4103, VVDS-7106 and VVDS-6913) are DD disks (filled symbols). Among the DD galaxies we highlighted using a filled square symbol, the galaxy VVDS-6913 which is consistent with being the relic of a major merging event. And using a filled triangle, the galaxy VVDS-7106 for which the error on the  $V_{rot}$  is extremely high.

We also infer the ratios of the maximum velocity over the local velocity dispersion  $V_{rot}/\sigma_0$  in order to characterize the dominance of the rotation versus the disordered motions of the gas. We determine the ratio  $r_c/r_{gas}$  between the ra-

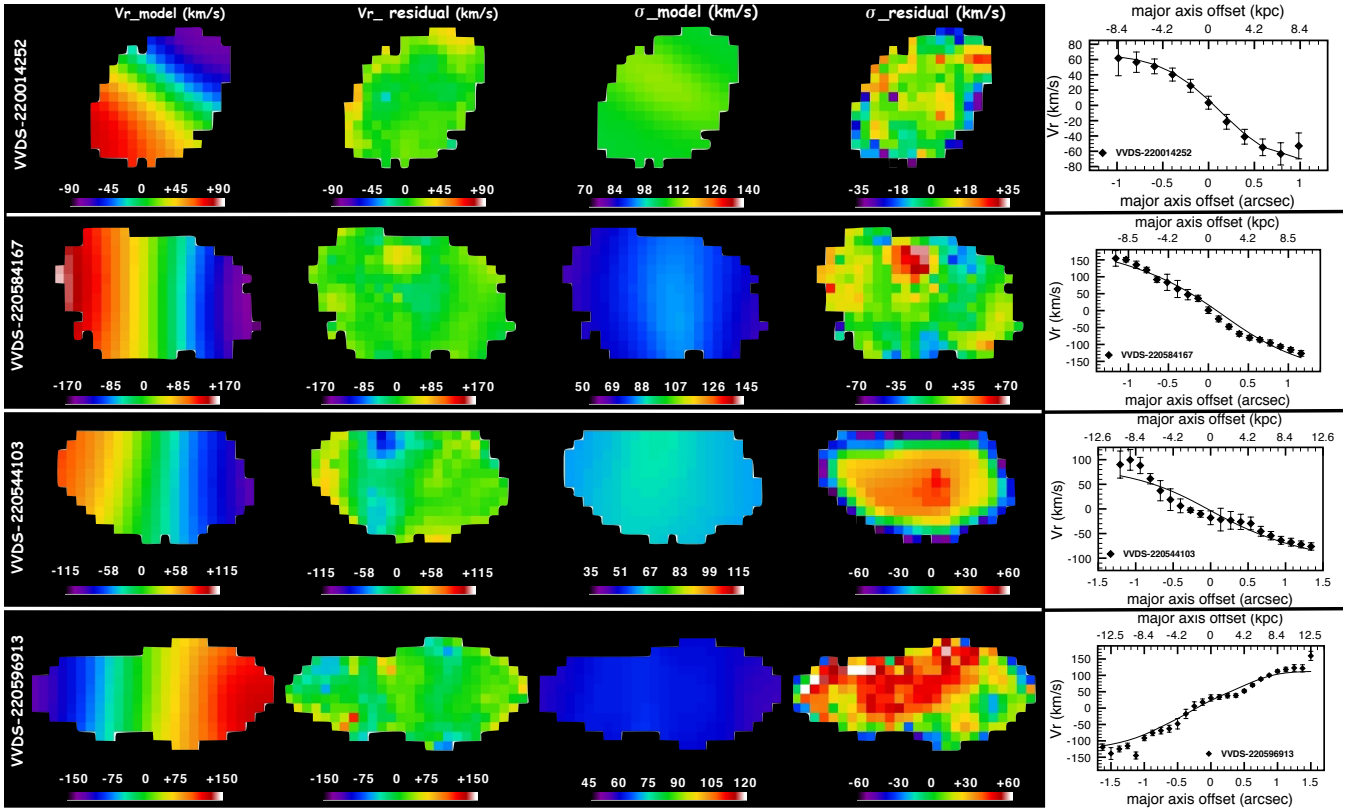


**Figure 6.** Kinematic best-fit models of galaxies of our sample (left panel) for both the velocity and the dispersion, after adding the effect of the beam smearing. The difference for both the velocity and the dispersion between the observed map and the best-fit model map is also shown and may display non-negligible random motions in the gas. An one-dimensional rotation curve extracted using an ‘idealized’ slit from the observed H $\alpha$  velocity map, overlaid with the best-fitting model, is shown in the right panel.

dius of the plateau, as estimated by the rotation modelling, and the radius of nebular emission detected in the SINFONI data to emphasize how close or far to the centre the maximum of the velocity is reached. We discuss this two ratios for each galaxy in section 5. The values for  $V_{rot}/\sigma_0$ ,  $r_c/r_{gas}$  and the classification are shown in Table 7.

For objects where the velocity shear is well fitted by the simple rotation model, we compute the dynamical masses assuming that the object is a circularly rotating disk. Thus the total mass within  $r_c$  for which the maximum rotational velocity  $V_{rot}$  is reached, is approximately described by:

$$M_{dyn} = V_{rot}^2 r_c / G \quad (9)$$

where  $V_{rot}$  has been correction for inclination effects. Both this asymptotic velocity, and the radius of the turnover ( $r_c$ ) are inferred from our model fits to the observed velocity maps to correct for the the effect of beam-smearing (due to the seeing). The results are given in Table 7.

We also computed the Toomre parameter ‘ $Q$ ’ (Toomre 1964) which is used to quantify the stability of the disk against gravitational collapse. Typically, values of  $Q > 1$  represent dynamically stable systems for which the total baryonic mass can be supported by the observed rotational motion alone, while values of  $Q < 1$  suggest that the observed baryonic total mass exceeds that which can be supported by the observed rotational velocity of the disk, indicating either that the disk itself is unstable or that non-rotational motions contribute a significant degree of support

to the system. Finally,  $Q \sim 1$  represents the case of marginal stability. In order to estimate ‘ $Q$ ’, we considered the ratio of masses within the radius probed by the SINFONI detections ( $r_{disk} = r_{gas}$ ) and therefore computed the dynamical masses within the gas radius. We do not take the values of the dynamical masses computed from the rotationally-supported thin disk model ( $M_{dyn}$ ). The total baryonic mass is  $M_{disk} = M_{gas} + M_*$ . We thus used the following relation:

$$Q = \frac{V_{rot}^2}{GM_{disk}/r_{disk}} = \frac{V_{rot}^2}{G(M_{star} + M_{gas})/r_{gas}} \quad (10)$$

Results are given in Table 7.

## 5 DYNAMICAL PROPERTIES AND NATURE OF INDIVIDUAL GALAXIES

In this Section, we summarize the properties of each galaxy, derived from its spectral energy distribution, mass, star formation rate and dynamical structure. We use this to provide an insight into the nature and evolutionary status of each the 10 galaxies in our sample.

### 5.1 VVDS-1235

This galaxy has the lowest redshift of our sample and the lowest stellar mass ( $\sim 0.6 \times 10^{10} M_\odot$ ). It exhibits complex kinematics, and it is impossible to find a clear centre for this

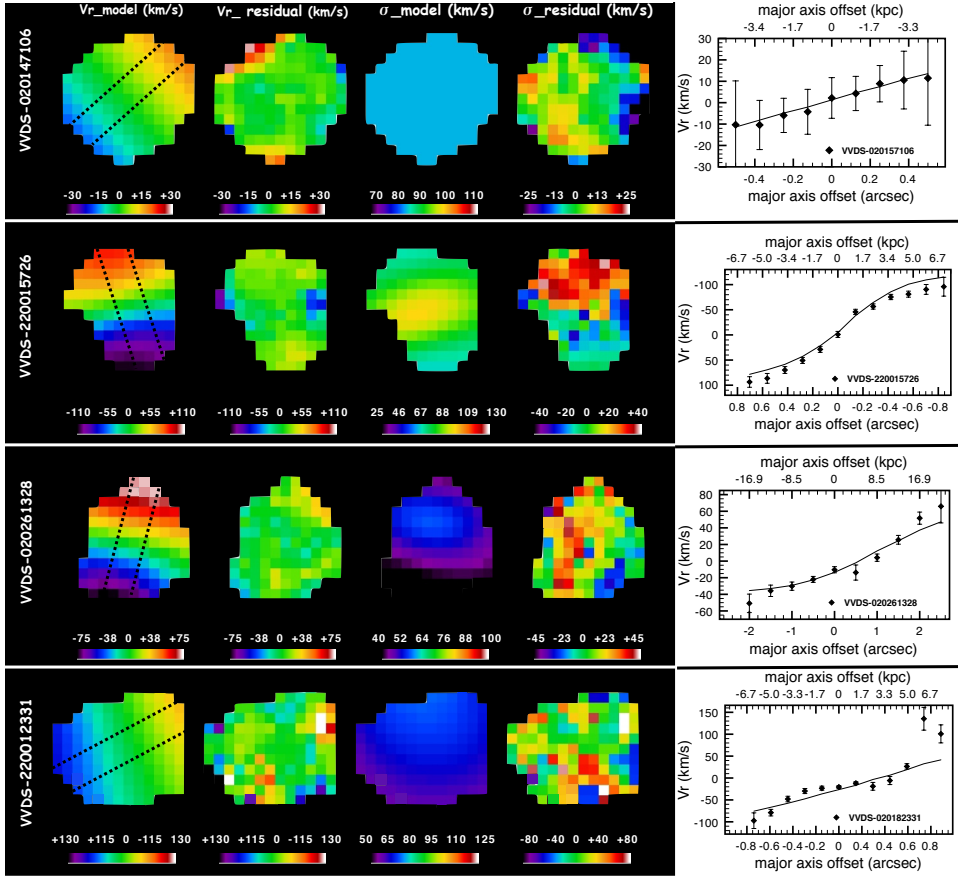


**Figure 7.** Similar as Fig.6 for four other galaxies.

clumpy galaxy. Its  $\sigma$ -map shows several peaks which seem to match with the knots in the  $H\alpha$  intensity map. The peak with the maximum  $H\alpha$  flux shows a very high dispersion of  $\sim 240 \text{ km s}^{-1}$ . Our simple rotating disk model did not succeed in reproducing its complex velocity field; we interpret this galaxy as being a merging system.

## 5.2 VVDS-2331

This galaxy shows a velocity gradient of  $\pm 50 \text{ km s}^{-1}$  in the south-west/north-east direction (position angle:  $-69^\circ$ ). However, we only cover the central part since the plateau is not reached in our SINFONI observation. Its  $\sigma$ -map show a peak at  $120 \text{ km s}^{-1}$  slightly shifted from the  $H\alpha$  flux peak. However this peak also corresponds to a region with high noise. The rotational disk model fits the observed inner gradient relatively well, and we found a plateau velocity, corrected from beam smearing, of  $V_{rot} \sim 197 \text{ km s}^{-1}$  within 4.8 kpc. We found a virial mass of  $\sim 6 \times 10^{10} M_\odot$  and a dynamical mass of  $\sim 0.4 \times 10^{10} M_\odot$ , estimated from the  $V_{rot}$  inferred by the rotation modelling. It is one of the objects for which we found the lowest value of local velocity dispersion ( $< 40 \text{ km s}^{-1}$ ), leading to a  $V_{rot}/\sigma_0 \sim 5$ . VVDS-2331 also seems to have a large amount of gas ( $\mu \sim 70\%$ ), a high SFR and a young stellar population. It is therefore a good candidate for being a cold rotating disk ( $Q \sim 3$ ), where rapid star formation is occurring due to the injection of large quantities of cold gas.

## 5.3 VVDS-6913

The  $H\alpha$ -map shows two components, one of which is coincident with the peak of the  $H\alpha$  flux. However, the kinematical centre is located exactly between the two components, at  $\sim 8 \text{ kpc}$  from the centre of the main blob. It has a smooth velocity gradient and a large peak in the centre of its  $\sigma$ -map. The whole velocity map, including the two blobs, is well fitted by the rotation model (plateau velocity of  $\sim 139 \text{ km s}^{-1}$  reached at 10.7 kpc and  $V_{rot}/\sigma_0 \sim 3$ ). However the small arms linked to the large peak in the  $\sigma$ -map reveal a perturbed rotation. The peak of the dispersion and the arms are still visible in the residual map of the dispersion (see Fig. 6), which emphasize additional random motions (up to  $70 \text{ km s}^{-1}$  with a mean of  $20 \text{ km s}^{-1}$ ). This morphology can also be explained by the presence of a relic of a previous merger event, or by being a clumpy disk galaxy. VVDS-6913 has the second highest virial mass ( $\sim 20 \times 10^{10} M_\odot$ ) and dynamical mass ( $\sim 5 \times 10^{10} M_\odot$ ) of the galaxies in our sample. It has a reasonable SFR and also a sizeable stellar mass ( $\sim 4 \times 10^{10} M_\odot$ ) and the remaining quantity of gas ( $\mu < 35\%$ ) indicates that it has already turned a large amount of its gas into stars. We classify it as a DD rotating disk, since its disk stability appears marginal ( $Q \sim 2$ ).

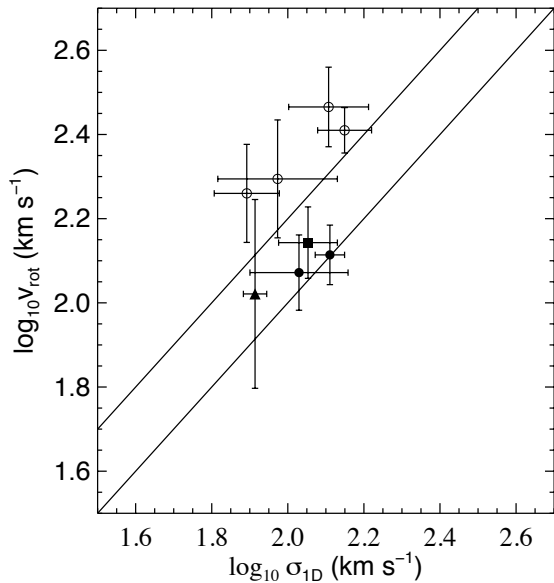


**Figure 5.** Maximum velocity from rotation modeling ( $\log V_{rot}$ ) vs integrated line width ( $\log \sigma_{1D}$ ). *open circle*: RD rotating disks and *filled symbols*: DD rotating disks. Among the DD rotating disks we highlighted in *filled triangle*: VVDS-7106, and in *filled square*: VVDS-6913. The lines are the 1:1 line and the Rix et al. (1997)  $\sigma = 0.6V_c$  line.

#### 5.4 VVDS-5726

This nearly edge-on galaxy has its H $\alpha$ -map and  $\sigma$ -map peaked at the centre. The general shape of the velocity gradient is well reproduced by the rotational disk model with a maximum velocity of  $V_{rot} \sim 292 \text{ km s}^{-1}$  reached at 1.5 kpc and a local velocity dispersion of  $\sim 60 \text{ km s}^{-1}$  ( $V_{rot}/\sigma_0 \sim 5$ ). We found a virial mass of  $\sim 9 \times 10^{10} M_\odot$  and a dynamical mass of  $\sim 3 \times 10^{10} M_\odot$  for this object. This galaxy has the highest stellar mass ( $\sim 4 \times 10^{10} M_\odot$ ), the lowest gas fraction ( $< 30\%$ ) and one of the oldest stellar population (1.26 Gyr) of all the objects in our sample. Also taking into account its moderate SFR, we believe that this galaxy has a rotating disk of cold gas ( $Q \sim 3$ ) and it is at a later evolutionary state than most of the objects in our sample.

#### 5.5 VVDS-4252

The resolved velocity structure present a smoothly varying shear along the major axis, including the beginning of a plateau at a radial velocity of  $\sim \pm 54 \text{ km s}^{-1}$ . There is a very good agreement between the best-fit rotating disk model, with a maximum  $V_{rot} \sim 130 \text{ km s}^{-1}$  reached at 4.5 kpc, and the observed rotation curve (see Fig. 7). The residual maps show very low mean and rms values (see Table 6). However, the velocity dispersion map is broadly peaked at the centre of the galaxy and the high value local velocity dispersion ( $\sim 100 \text{ km s}^{-1}$ ) probably indicates that the galaxy does not have a dynamically cold rotating disk of ionized gas, due to significant disordered motion in the gas ( $V_{rot}/\sigma_0 \sim 1$ ). We also found that the virial mass ( $\sim 14 \times 10^{10} M_\odot$ ) is much higher than the dynamical mass ( $\sim 2 \times 10^{10} M_\odot$ ).

It has a young stellar population, a very high gas fraction ( $\sim 87\%$ ) and seems to be undergoing a strong episode of star formation. VVDS-4252 is probably consistent with a rotation in a heated disk (DD unstable rotating disk ( $Q \sim 0.4$ )).

#### 5.6 VVDS-4103

This galaxy has a velocity gradient which can be fitted by a simple rotating disk model, and presents a clear peak in its  $\sigma$ -map which corresponds to the maximum of the H $\alpha$  flux distribution. The best-fit disk model indicates a maximum velocity of  $V_{rot} \sim 118 \text{ km s}^{-1}$  km/s, reached at 8.5 kpc and a local velocity dispersion of  $\sim 58 \text{ km s}^{-1}$ . However, the peak in the residual dispersion map (see Fig. 7) and the low ratio  $V_{rot}/\sigma_0 \sim 2$  indicates the presence of non-negligible random motions in the gas. We also found that the virial mass ( $\sim 12 \times 10^{10} M_\odot$ ) is much higher than the dynamical mass ( $\sim 3 \times 10^{10} M_\odot$ ). It has an extremely high SFR and gas fraction. VVDS-4103 must be experiencing a very strong burst of star formation, which might be the cause of non-negligible random motions of the gas peaked at the centre of the object. These galaxy properties are quite similar to the properties of VVDS-4252 and we also classify it as a DD unstable rotating disk ( $Q \sim 0.3$ ).

#### 5.7 VVDS-4167

This galaxy exhibits a smoothly varying shear along its major axis and has a clear peak in its  $\sigma$ -map corresponding to the maximum of the H $\alpha$  flux distribution which is slightly shifted from the centre of the object. The velocity field is relatively well fitted by our simple rotational disk model with a maximum velocity of  $V_{rot} \sim 257 \text{ km s}^{-1}$  km/s, reached at 10.8 kpc, and a local velocity dispersion of  $\sim 54 \text{ km s}^{-1}$ . This leads to a  $V_{rot}/\sigma_0 \sim 5$  showing the dominance of the rotation over the random motions of the gas, even if the peak near the centre is also visible in the residual of the dispersion map (see Fig. 7). We found a virial mass of  $\sim 26 \times 10^{10} M_\odot$  and a dynamical mass of  $\sim 17 \times 10^{10} M_\odot$  for this object. It also has a sizeable and very young stellar population, a reasonable SFR and has turned slightly more than half of its gas into stars. We believe therefore that this galaxy can be consistent with a cold rotating disk ( $Q \sim 8$ ).

#### 5.8 VVDS-7106

This galaxy seems to have a low velocity shear (see Fig. 3). As with VVDS-2331, we cover only the central part of this object and therefore the plateau has not been reached. The rotational disk model fits the observed inner gradient relatively well and gives an estimated maximum velocity of  $V_{rot} \sim 105 \text{ km s}^{-1}$  km/s, reached at 9.4 kpc, and a local velocity dispersion of  $\sim 82 \text{ km s}^{-1}$ . We also found that the virial mass ( $\sim 4 \times 10^{10} M_\odot$ ) is similar to the dynamical mass ( $\sim 2 \times 10^{10} M_\odot$ ), and that it has a ratio of  $\frac{r_c}{r_{gas}} > 1$ . We measure a low ratio of  $V_{rot}/\sigma_0 \sim 1$ , showing the dominance of random motions in the gas as also indicated by the high local velocity dispersion. VVDS-7106 has the lowest stellar mass in our sample and an extremely young stellar population. More than 60% of its gas has been turned into star

and it has an average SFR. Taking into account all of its properties, we classify it as a DD rotating disk despite its marginal stable disk ( $Q \sim 1$ ).

### 5.9 VVDS-6027

This object has a young stellar population with an average stellar mass of  $\sim 1 \times 10^{10} M_{\odot}$ , a low gas fraction of ( $< 35\%$ ) and a small SFR. It presents an  $H\alpha$  flux distribution with a peak located at its centre and a low surface brightness emission tail seen also in the stellar population image (see Fig. 4). This galaxy is relatively well-resolved but shows no strong evidence for spatially resolved velocity structure. We classify it as featureless (perhaps consistent with being a face-on galaxy).

### 5.10 VVDS-1328

As for VVDS-5726, this nearly edge-on galaxy has a velocity gradient which is well reproduced by the rotational disk model. However, the peak seen in the  $\sigma$ -map is slightly shifted from the peak in the  $H\alpha$  flux map (see Fig. 3). The best-fit disk model indicates a maximum velocity of  $V_{rot} \sim 182 \text{ km s}^{-1}$ , reached at 0.5 kpc, and a local velocity dispersion of  $\sim 36 \text{ km s}^{-1}$  ( $V_{rot}/\sigma_0 \sim 5$ ). We found a virial mass of  $\sim 3 \times 10^{10} M_{\odot}$  and a dynamical mass of  $\sim 0.4 \times 10^{10} M_{\odot}$  for this object. This galaxy has an average stellar mass of  $\sim 1 \times 10^{10} M_{\odot}$ , a low gas fraction of ( $< 35\%$ ) and a small SFR. We believe that this ‘mature’ galaxy has a rotating disk of cold gas ( $Q \sim 6$ ).

## 6 DISCUSSION

Here, we study and discuss the relations between the kinematical and physical properties of the ionized gas and the physical properties of the stellar population for the 10 galaxies of our sample.

### 6.1 Relations between the recent-to-past star formation rate and other properties

We calculated the recent-to-past star formation rate ratio ( $SFR_{corr}/SFR_{sed}$ ), which is the ratio between the star formation rate estimated from the ionized gas (using the  $H\alpha$  emission) and the one estimated from the best-model SED fitting (both of which have been dereddened).  $SFR_{sed}$  is averaged on a timescale ten times longer than the  $SFR_{corr}$ , which is an indication of the instantaneous star formation. Given these different timescales, the ratio between the two estimates gives information on the presence of recent burst of star formation above the standard continuous declining star formation. We investigated, thus, the correlation between the recent-to-past star formation rate ratio ( $SFR_{corr}/SFR_{sed}$ ) and the gas mass fraction and the stellar mass.

#### 6.1.1 Relations between the recent-to-past star formation rate ratio and the gas mass fraction

In Fig. 8, we plot the recent-to-past SFR ratio vs. the gas mass fraction for the 10 galaxies of our sample. We

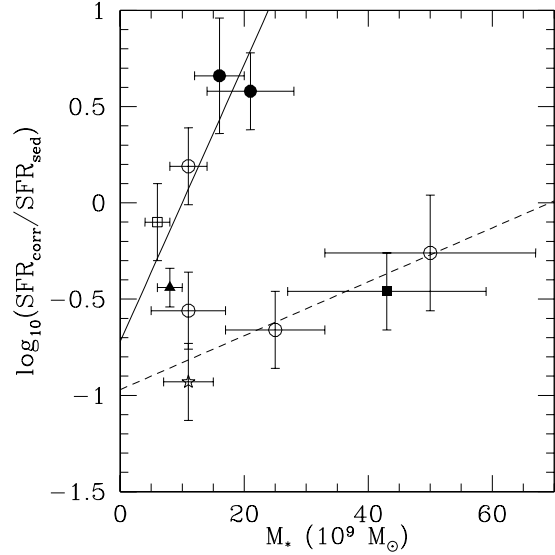


**Figure 8.** Relation between the recent-to-past star formation rate ratio and the gas mass fraction. The symbols give the dynamical classification as follows: *open circle*: RD rotating disks; *filled symbols*: DD rotating disks, with in particular *filled triangle*: VVDS-7106, and *filled square*: VVDS-6913; *star*: featureless. We found two classes (see text) and a least-square linear fit is performed for each of them.

found that only galaxies with a significant amount of gas ( $\mu \sim > 0.6$ ), are undergoing episodes of strong star formation (bursts). From Fig. 8, a correlation between the recent-to-past SFR ratio and the gas mass fraction, given that we divide the sample into two classes is therefore clearly seen. The first one include the three objects which have the smallest recent-to-past SFR ratio. These three objects are: the face-on/featureless VVDS-6027 (star symbol), the DD rotating galaxy VVDS-7106 (filled triangle), and the RD rotating galaxy VVDS-4167 (open circle), and therefore are not showing evidence of bursts of star formation. This first class seems to follow the relation (least square fit):

$$\log_{10}(SFR_{corr}/SFR_{sed}) = 1.38(\pm 0.45) \times \mu - 1.40(\pm 0.24),$$

and the second class, all the remaining objects, seems to follow the relation:

$$\log_{10}(SFR_{corr}/SFR_{sed}) = 1.77(\pm 0.01) \times \mu - 1.03(\pm 0.01).$$

Can these two classes be related to underlying kinematical properties? We find indeed that the ratio of the kinematical radius to the gas radius ( $r_c/r_{gas}$ , see Table 7) has a mean value of  $0.40 \pm 0.01$  for the galaxies with a high recent-to-past SFR ratio, and  $0.94 \pm 0.01$  for the three others of the first class. It appears, thus, that the rather intuitive relation between the amount of recent star formation and the amount of ionized gas depends strongly on kinematics. ‘Slow rotator’ (intermediate redshift galaxies with a  $r_c/r_{gas} > 0.6$ ) appear less efficient in converting a high mass fraction of ionized gas into a burst of star formation. This will have to be confirmed and refined with better data and more objects.

**Table 7.** Kinematical properties

Galaxy	$v_{shear}$	$V_{rot}/\sigma_0$	$M_{vir}$ (1)	$M_{dyn}$ (1)	$\frac{r_c}{r_{gas}}$	$Q$ (2)	dyn. class (3)
VVDS-1235	$92 \pm 13$	-	$4 \pm 2$	-	-	-	merger.
VVDS-2331	$99 \pm 17$	$5.1 \pm 2.9$	$6.4 \pm 2.9$	$0.4 \pm 0.7$	$0.52 \pm 0.87$	$3.3 \pm 0.9$	RD
VVDS-6913	$139 \pm 7$	$3.2 \pm 0.8$	$20 \pm 6.5$	$5 \pm 3$	$0.53 \pm 0.15$	$2.4 \pm 0.6$	DD
VVDS-5726	$95 \pm 9$	$4.9 \pm 0.5$	$8.7 \pm 0.3$	$3 \pm 4$	$0.22 \pm 0.3$	$3.3 \pm 0.5$	RD
VVDS-4252	$54 \pm 9$	$1.3 \pm 0.1$	$14 \pm 8.7$	$2 \pm 1$	$0.42 \pm 0.19$	$0.4 \pm 0.7$	DD
VVDS-4103	$83 \pm 16$	$2.0 \pm 0.7$	$12 \pm 13$	$3 \pm 2$	$0.63 \pm 0.23$	$0.3 \pm 0.8$	DD
VVDS-4167	$140 \pm 8$	$4.8 \pm 0.8$	$26 \pm 2.2$	$17 \pm 5$	$0.65 \pm 0.13$	$7.5 \pm 0.5$	RD
VVDS-7106	$12 \pm 14$	$1.3 \pm 0.4$	$4.1 \pm 0.7$	$2 \pm 3$	$1.22 \pm 0.58$	$1.4 \pm 1.0$	DD
VVDS-6027	$<10 \pm 11$	-	$1 \pm 0.5$	-	-	-	f.l.
VVDS-1328	$58 \pm 8$	$5.1 \pm 0.7$	$3.4 \pm 1.0$	$0.4 \pm 3$	$0.07 \pm 0.56$	$5.7 \pm 0.7$	RD

The columns are as follows: (1)  $10^{10} M_\odot$ ; (2) Toomre parameter (Toomre 1964); (3) dynamical classification: RD for *rotation-dominated* rotating disk, DD for *dispersion-dominated* rotating disk, and f.l. for *featureless*.

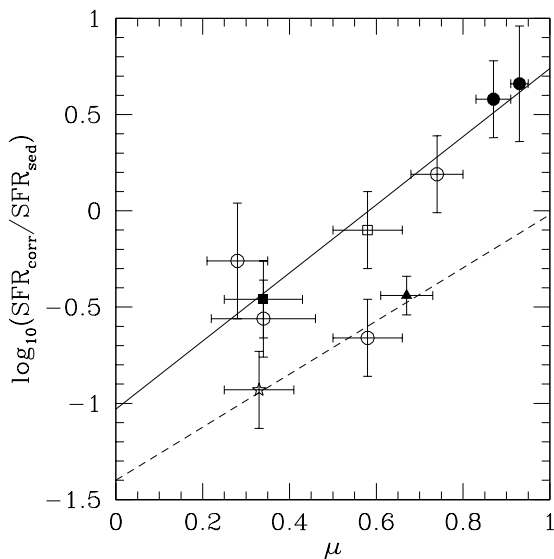


**Figure 9.** Relation between the recent-to-past star formation rate ratio and the logarithm of the stellar mass. The symbols are the same than in Fig. 8

### 6.1.2 Relations between the recent-to-past star formation rate ratio and the stellar mass

In Fig. 9, we plot the recent-to-past SFR ratio vs. the stellar mass for the 10 galaxies of our sample. We found that the galaxies of our sample need higher stellar masses to reach higher recent star formation rates. The recent star formation to stellar mass efficiency is moreover significantly stronger for half of our sample. From Fig. 9, we see two possible correlations between the recent-to-past SFR ratio and the stellar mass. The first class includes objects dominated by recent star formation ( $SFR_{corr}/SFR_{sed} > 1$ ): the merger object and all DD galaxies, except VVDS-6913 with the following relation (least squares fit):

$$\log_{10}(SFR_{corr}/SFR_{sed}) = 0.072(\pm 0.05) \times M_*(10^9 M_\odot) - 0.72(\pm 0.4)$$

The second class includes objects dominated by past star formation ( $SFR_{corr}/SFR_{sed} < 1$ ): the featureless object

and all RD galaxies, except VVDS-2331, seems to follow the relation (least squares fit)

$$\log_{10}(SFR_{corr}/SFR_{sed}) = 0.014(\pm 0.03) \times M_*(10^9 M_\odot) - 0.97(\pm 0.7)$$

The star formation to stellar mass efficiency is moreover stronger for objects experiencing a burst of recent star formation, and appears also to be related to the dominance of random motions in the gas. We indeed notice that the ratio of the maximum velocity to the velocity dispersion ( $V_{rot}/\sigma_0$ ; see Table 7) is different for the rotating disks galaxies inside the two classes: it has a mean value of  $2.42 \pm 0.5$  for the first class, and  $4.5 \pm 0.3$  for the second one. We thus propose to refine our classification: disk galaxies of the first family would be called "hot/perturbed rotators", while the disk galaxies of the second family would be 'cold rotators'. Only hot rotators and objects dominated by random motions, like the merger seem to be able to experience a recent burst. The separation between cold rotators and hot/perturbed rotators would then be  $V_{rot}/\sigma_0 \approx 4$ . This also will have to be confirmed and refined with better data and more objects.

## 6.2 The stellar mass Tully-Fisher relation

In Fig. 10, we show the Tully-Fisher relations for the  $1.2 \lesssim z \lesssim 1.5$  galaxies showing evidence of rotation. In the top panel, we plotted the stellar mass versus the maximum velocity. As can be seen, there is a clear separation between the RD rotating disks (open circle) from the DD rotating disks (filled symbols). However, both groups of objects suggest a good correlation between the stellar mass and the rotation maximum speed similar to that seen in the local universe (solid line). By assuming the local slope of the Tully-Fisher relation from (Bell & de Jong 2001), we found a best fitting zero point of  $-0.29 \pm 0.25$  for the RD galaxies and  $0.90 \pm 0.43$  for the DD galaxies.

In the bottom panel of Fig. 10, we replace the maximum velocity by the  $S_{0.5}$  index ( $0.5V_{rot}^2 + \sigma_0^2$ )<sup>0.5</sup>, which allows the disordered motions in the gas to be taken into account (Kassin et al. 2007). The separation between the RD rotating disks and the DD rotating disks is less obvious while adding the disordered motions. It seems that we also detect an evolution of the relation since  $z \sim 1$  (which is shown as the solid line in Fig. 10).

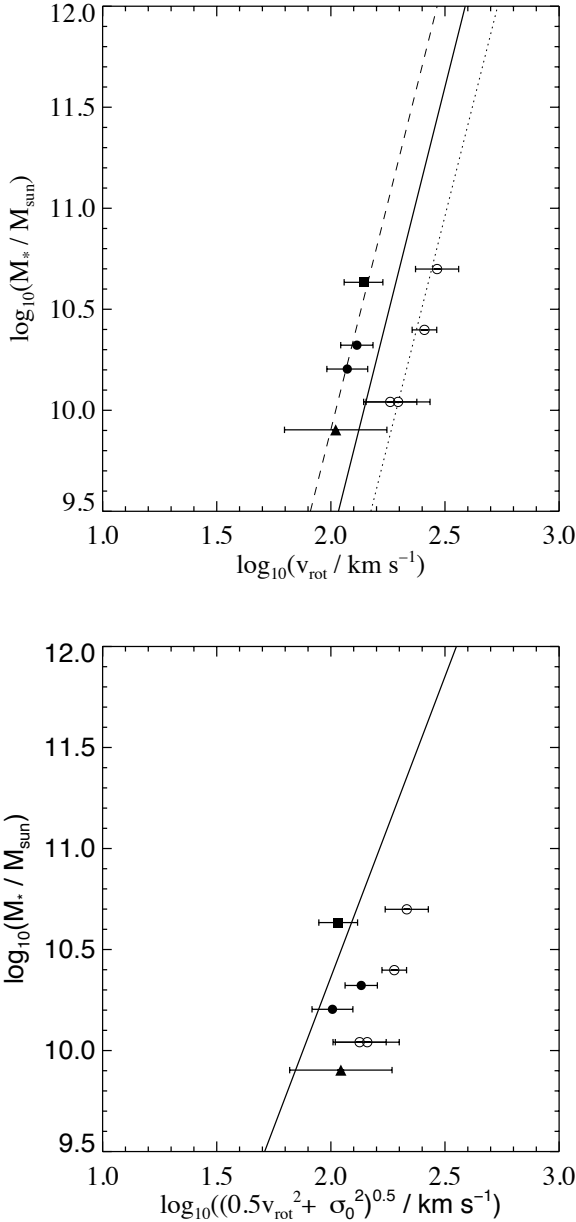


**Figure 10.** The stellar mass Tully-Fisher relation at  $1.2 < z < 1.5$ , using the maximum velocity (top panel) and using the  $S_{0.5}$  index (bottom panel;  $(0.5V_{rot}^2 + \sigma_0^2)^{0.5}$ ). In the top panel, the solid line is the local relation from (Bell & de Jong 2001), while in the bottom panel it is the  $z \sim 1$  relation from (Kassin et al. 2007). The symbols are *open circle*: RD rotating disks and *filled symbols*: DD rotating disks with in particular *filled triangle*: VVDS-7106, and *filled square*: VVDS-6913.

**6.3 Comparison with theoretical studies, with results from other intermediate- and high-redshift samples**

Previous studies at  $z > 2$  have shown the presence of large quantity of gas in comparison to the stellar population in high-redshift galaxies (Law et al. 2009; Lemoine-Busserolle et al. 2009). We found that six out of then galaxies of our sample have a gas fraction higher than 0.50. The typical

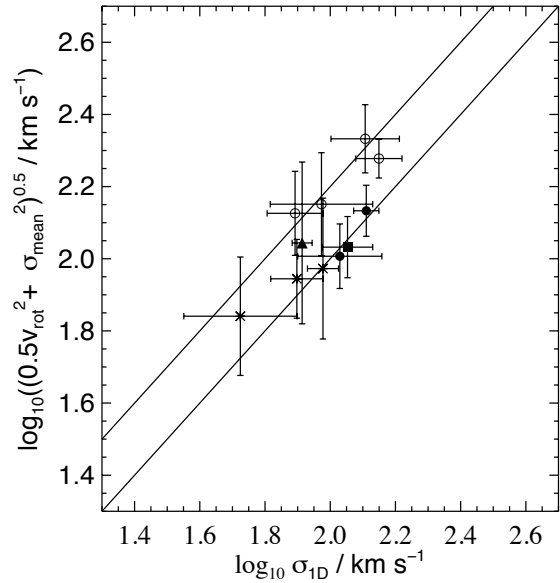


**Figure 11.** Combined velocity ( $S_{0.5}$ ) versus integrated linewidth velocity dispersion. The diagonal lines are the same as in Wright et al. (2007), i.e. a 1 : 1 line and the Rix et al. (1997)  $\sigma = 0.6V_c$  line ( $V_c$  is the circular velocity). Linewidth  $\sigma_{1D}$  and  $S_{0.5}$  are correlated; the 0.5 pre-factor makes the combined velocity width a better estimate of velocity dispersion, so that the correlation is tighter and the galaxies closer to the 1 : 1 line. The symbols are *open circle*: RD rotating disks and *filled symbols*: DD rotating disks with in particular *filled triangle*: VVDS-7106, and *filled square*: VVDS-6913; *asterisk*:  $z \sim 3$  galaxies from Lemoine-Busserolle et al. (2009)

$v/\sigma$  for our sample is similar to the one found for the SINS galaxies ( $\sim 2 - 4$ ; Förster Schreiber et al. (2006); Genzel et al. (2006, 2008)), but more higher than the values found by Lemoine-Busserolle et al. (2009) ( $\sim 0.4 - 1.5$ ) and Law et al. (2009) galaxies at  $z \sim 2$  ( $\sim 0.8$ ). Lemoine-Busserolle et al. (2009) found in their sample, 3 galaxies showing the presence of rotation. Fig 11 plots the combined velocity scale  $S_{0.5}$  against the 1D linewidth  $\sigma_{1D}$  for our sample together with this three galaxies at  $z \sim 3 - 4$ . It should give an idea of the evolution of the dynamical mass which take also into account the contribution from the random motions in the gas. Fig 11 shows an increase of the dynamical mass for  $z \sim 3 - 4$  to  $z \sim 1.3 - 1.5$  for the DD disks.

Despite the low resolution of the morphological data (CFHTLS I-band images) which shows that, except VVDS-1235, all the galaxies seems to be disk like objects with a central bulge, the IFU data obtained on the sample of the 10 star-forming galaxies at  $1.0 \lesssim z \lesssim 1.5$  have confirmed the presence of a velocity gradient resembling that expected for an internally rotating system, but has also reveals the presence of non-negligible random motions in the gas. Recent studies at the same redshift have found similar results. Bournaud et al. (2008) have study a clumpy galaxy at  $z = 1.6$ , which was previously classified as an on-going merger. Their study reveals that the kinematics properties (the large-scale rotation with  $V_{rot} \sim 100 \text{ km s}^{-1}$ ), the stellar properties (young age, stellar mass range) and the properties of the gas are very similar to those of the galaxies of our sample

(in particular VVDS-6913). Their numerical model shows that a such turbulent rotation disk, results more from the evolution of an unstable gas-rich disk galaxy than from a merging event. (Wright et al. 2007, 2009; Bournaud et al. 2008)

Five of the rotating disk of our sample have a  $Q > 2$ , which indicates the stability of their disk. Can this large stable disk systems evolve in present-day thin disks? We already note that the disk galaxies in our sample (except the two galaxies VVDS-1328 and VVDS-5726 which already have similar properties to that of the present-day local spirals) possess a large disk of gas and younger stars (age  $< 1$  Gyr), which can further grow in mass by continued accretion. The lack of rotation observed in this objects in comparison to the thin local disk is nowadays well known and taken into recent plausible formation and evolution of high-redshift thick disk models. These scenarios can predict that on the largest scales a velocity gradient tracing a rotation can be observed with high velocity dispersion. They also shown that before  $z \sim 2$  the hot mode of accretion dominates, but after  $z \sim 2$ , the galaxy has a thin and extended disk component with  $Q \simeq 1.5 - 2$ , which indicates that the disk is marginally stable. They indicate also that after these earlier stages the galaxy enters a slow accretion phase and the disk evolves quiescently until  $z = 0$  (Kereš et al. 2005; Dekel & Birnboim 2006; Ocvirk et al. 2008; Dekel et al. 2009a). The results presented in this paper support the hypothesis that stable gas-rich disks seen at intermediate and high-redshifts may internally evolve into present-day spirals.

## 7 CONCLUSIONS

We have presented the 2D kinematics and the physical properties of a sample of ten star-forming disk galaxies at  $1.0 \lesssim z \lesssim 1.5$ . Among these objects, three (VVDS-4252, VVDS-4103 and VVDS-4167) are undergoing a strong burst of star formation. We found mainly four kinematical types in our sample which are: one merger (VVDS-1235); one featureless (or face-on) galaxy (VVDS-6027); four DD rotating disks – VVDS-4252, VVDS-7106, VVDS-4103 and VVDS-6913 which is also consistent of being the relic on a major merging event (to which the disk system seems to have survived) or a good candidate for being a clumpy galaxy; and finally four other galaxies are RD disks – VVDS-2331, VVDS-4167, including VVDS-1328 and VVDS-5726 which are pure rotationally supported disks. These two rotating disks achieve a maximum velocity of  $\sim 180\text{-}290 \text{ km s}^{-1}$  km/s within  $\sim 0.5\text{-}1$  kpc, similar to local spirals with thin disk (Sofue et al. 1999). Regarding most of the DD rotating disk, they display a plateau velocity range of  $105\text{-}257 \text{ km s}^{-1}$  km/s, certainly underestimated due to beam smearing. However, their plateau radii (4.5-10.8 kpc) derived from our rotating disk model are significantly higher than those derived for pure rotating disks and local spiral galaxies. We did not find any trace of AGN in the 10 objects. The galaxies of our sample have a relatively young stellar population ( $< 1$  Gyr) and possess a range of stellar mass of  $0.6\text{-}5 \cdot 10^{10} M_{\odot}$ . In addition, most of them have not yet converted the majority of their gas into stars (six galaxies have their gas fraction  $> 50$  per cent). Therefore, the galaxies which already have a stable disk (six of them) would have their final stellar mass

similar to the present-day spirals, to which these rotating systems can be seen as precursors. We also investigated the stellar mass Tully-Fisher relation at  $1.2 \lesssim z \lesssim 1.5$  and found a scatter between the RD disk galaxies and the DD disk galaxies. We also found for this two groups of objects a change of the zero point in comparison with the stellar mass Tully-Fisher relation in the local universe, but this is speculative considering the statistics of our sample.

Although, we have presented results on the dynamical structure and the physical properties of a small sample of star-forming galaxies at  $1.0 \lesssim z \lesssim 1.5$ , we have been able to investigate the dynamical type and the physical properties of late-type objects at this intermediate redshifts. Increasing the samples at different redshift ranges for which near-infrared IFS data and multi-wavelength broad-band photometric data can be obtained, will definitely develop our understanding of the dynamical characteristics and nature of various systems (mergers, rotating disks, etc.) and therefore will lead us to understand how galaxies have evolved to match the present-day Hubble sequence.

## ACKNOWLEDGMENTS

We would like to thank Aprajita Verma and Andy Bunker for helpful discussions. We are very grateful to the VLT Observatory for accepting this programme. The authors also thank Markus Hartung for help obtaining the observations during the observing runs and Sebastian Sánchez for providing the code to create the kinematics maps from the 3D cube. The anonymous referee is greatly acknowledged for providing useful and constructive comments. The author wish to recognize and acknowledge the significant contribution the VVDS collaboration has done by providing the targets. In particular Thierry Contini who helped greatly with the targets selection. Part of this work was supported by the Marie Curie Research Training Network *Euro3D*; contract No. *HPRN-CT-2002-00305*. M. Lemoine-Busserolle is supported by the Gemini Observatory, which is operated by the Association of Universities for Research in Astronomy, Inc., on behalf of the international Gemini partnership of Argentina, Australia, Brazil, Canada, Chile, the United Kingdom, and the United States of America.

## References

- Bell, E. F., & de Jong, R. S. 2001, *ApJ*, 550, 212
- Bouché N., Cresci G., Davies R., Eisenhauer F., Förster Schreiber N. M., et al. 2007, *ApJ*, 671, 303
- Bournaud F., et al. 2008, *A&A*, 486, 741
- Calzetti D., 2001, *PASP*, 113, 1449
- Chabrier G., 2003, *PASP*, 115, 763
- Conselice C. J., Bundy K., Ellis R. S., Brichmann J., Vogt N. P., et al. 2005, *ApJ*, 628, 160
- Dekel A., Birnboim Y., 2006, *MNRAS*, 368, 2
- Dekel A. et al., 2009a, *Nature*, 457, 451
- Dekel A., Sari R., Ceverino D., 2009b, *ApJ*, 703, 785
- Dib S., Bell E., Burkert A., 2006, *ApJ*, 638, 797
- Erb, D. K., Steidel, C. C., Shapley, A. E., Pettini, M., Reddy, N. A., & Adelberger, K. L. 2006b, *APJ*, 647, 128
- Elmegreen B. G., Elmegreen D. M., 2005, *ApJ*, 627, 632

- Elmegreen, B. G., Elmegreen, D. M., Vollbach, D. R., Foster, E. R., & Ferguson, T. E. 2005, *ApJ*, 634, 101
- Elmegreen D. M., Elmegreen B. G., Ravindranath S., Coe D. A., 2007, *ApJ*, 658, 763
- Elmegreen B. G., Elmegreen D. M., Fernandez M. X., Lemonias J. J., 2009, *ApJ*, 692, 12
- Emsellem E., Monnet G., Bacon R., 1994, *A&A*, 285, 723
- Förster Schreiber N. M., Genzel R., Lehnert M. D., Bouché N., Verma A., et al. 2006, *ApJ*, 645, 1062
- Garilli B., Le Fèvre O., Guzzo L., Maccagni D., Le Brun V., et al. 2008, *A&A*, 486, 683
- Genzel R., Burkert A., Bouché N., Cresci G., Förster Schreiber N. M., et al. 2008, *ApJ*, 687, 59
- Genzel R., Tacconi L. J., Eisenhauer F., Förster Schreiber N. M., Cimatti A., et al. 2006, *Nature*, 442, 786
- Ilbert O., Arnouts S., McCracken H. J., Bolzonella M., Bertin E., et al. 2006, *A&A*, 457, 841
- Iovino A., McCracken H. J., Garilli B., Foucaud S., Le Fèvre O., et al. 2005, *A&A*, 442, 423
- Kassin S. A., Weiner B. J., Faber S. M., Koo D. C., Lotz J. M., et al. 2007, *ApJL*, 660, L35
- Kennicutt Jr. R. C., 1998, *ARA&A*, 36, 189
- Kereš D., Katz N., Weinberg D. H., & Davé R., 2005, *MNRAS*, 363, 2
- Law D. R., Steidel C. C., Erb D. K., Larkin J. E., Pettini M., et al. 2007, *ApJ*, 669, 929
- Law D. R., Steidel C. C., Erb D. K., Larkin J. E., Pettini M., et al. 2009, *ApJ*, 697, 2057
- Lawrence A., Warren S. J., Almaini O., Edge A. C., Hamblly N. C., et al. 2007, *MNRAS*, 379, 1599
- Le Fèvre O., Mellier Y., McCracken H. J., Foucaud S., Gwyn S., et al. 2004, *A&A*, 417, 839
- Le Fèvre O., Vettolani G., Garilli B., Tresse L., Bottini D., et al. 2005, *A&A*, 439, 845
- Lemoine-Busserolle M., Bunker A., Lamareille F., Kissler-Patig M., 2009, *MNRAS*, in press, (doi=10.1111/j.1365-2966.2009.15807.x; arXiv:0909.1386)
- McCracken H. J., Radovich M., Bertin E., Mellier Y., Dantel-Fort M., et al. 2003, *A&A*, 410, 17
- Nesvadba N. P. H., Lehnert M. D., Davies R. I., Verma A., Eisenhauer F., 2008, *A&A*, 479, 67
- Ocvirk P., Pichon C., Teyssier R., 2008, *MNRAS*, 390, 1326
- Oke J. B., Gunn J. E., 1983, *ApJ*, 266, 713
- Puech M., Flores H., Hammer F., Yang Y., Neichel B., et al. 2008, *A&A*, 484, 173
- Puech M., Hammer F., Flores H., Östlin G., Marquart T., 2006, *A&A*, 455, 119
- Queyrel J., et al. 2009, *A&A*, 506, 681
- Rix, H.-W., Guhathakurta, P., Colless, M., & Ing, K. 1997, *MNRAS*, 285, 779
- Salpeter E. E., 1955, *ApJ*, 121, 161
- Sánchez S. F., Becker T., Garcia-Lorenzo B., Benn C. R., Christensen L., et al. 2005, *A&A*, 429, L21
- Sánchez S. F., Becker T., Kelz A., 2004, *Astronomische Nachrichten*, 325, 171
- Sánchez S. F., Garcia-Lorenzo B., Mediavilla E., González-Serrano J. I., Christensen L., 2004, *ApJ*, 615, 156
- Shapiro K. L., et al. 2008, *ApJ*, 682, 231
- Sofue, Y., Tutui, Y., Honma, M., Tomita, A., Takamiya, T., Koda, J., & Takeda, Y. 1999, *ApJ*, 523, 136
- Temporin S., Iovino A., Bolzonella M., McCracken H. J., Scodggio M., et al. 2008, *A&A*, 482, 81
- van Starckenburg L., van der Werf P. P., Franx M., Labbé I., Rudnick G., et al. 2008, *A&A*, 488, 99
- Weiner B. J., Willmer C. N. A., Faber S. M., Melbourne J., Kassin S. A., et al. 2006, *ApJ*, 653, 1027
- Wright S. A., Larkin J. E., Barczys M., Erb D. K., Iserlohe C., et al. 2007, *ApJ*, 658, 78
- Wright S. A., Larkin J. E., Law D. R., Steidel C. C., Shapley A. E., et al. 2009, *ApJ*, 699, 421